

# Important Notice to Authors

**No further publication processing will occur until we receive your response to this proof.**

Attached is a PDF proof of your forthcoming article in *Physical Review D*. The article accession code is DD12983.

Please note that as part of the production process, APS converts all articles, regardless of their original source, into standardized XML that in turn is used to create the PDF and online versions of the article as well as to populate third-party systems such as Portico, Crossref, and Web of Science. We share our authors' high expectations for the fidelity of the conversion into XML and for the accuracy and appearance of the final, formatted PDF. This process works exceptionally well for the vast majority of articles; however, please check carefully all key elements of your PDF proof, particularly any equations or tables.

Figures submitted electronically as separate files containing color appear in color in the online journal. However, all figures will appear as grayscale images in the print journal unless the color figure charges have been paid in advance, in accordance with our policy for color in print (<https://journals.aps.org/authors/color-figures-print>).

## Specific Questions and Comments to Address for This Paper

The numbered items below correspond to numbers in the margin of the proof pages pinpointing the source of the question and/or comment. The numbers will be removed from the margins prior to publication.

- 1 Please check carefully throughout that editing has not changed the intended meaning.
- 2 Please define SXS in Table caption I.
- 3 There do not appear to be blue or red elements in Fig. 5. Please check.
- 4 In order to properly identify funding information, APS asks that all acronyms in the acknowledgments section be spelled out in full. Please check.
- 5 Please review the funding information section of the proof's cover letter and respond as appropriate. We must receive confirmation that the funding agencies have been properly identified before the article can publish.
- 6 This query was generated by an automatic reference checking system. Reference [26] could not be located in the databases used by the system. While the reference may be correct, we ask that you check them so we can provide as many links to the referenced articles as possible.
- 7 NOTE: External links, which appear as blue text in the reference section, are created for any reference where a Digital Object Identifier (DOI) can be found. Please confirm that the links created in this PDF proof, which can be checked by clicking on the blue text, direct the reader to the correct references online. If there is an error, correct the information in the reference or supply the correct DOI for the reference. If no correction can be made or the correct DOI cannot be supplied, the link will be removed.
- 8 A check of online databases revealed a possible error in Ref. c5. The page number has been changed from '074001' to '115012'. Please confirm this is correct.
- 9 A check of online databases revealed a possible error in Ref. c15. The page number has been changed from '85' to '425'. Please confirm this is correct.
- 10 Please check and confirm updated Refs. [53,62,64,113,128,132,139,140].
- 11 A check of online databases revealed a possible error in Ref. c88. The page number has been changed from '31323158' to '3132'. Please confirm this is correct.

## Titles in References

The editors now encourage insertion of article titles in references to journal articles and e-prints. This format is optional, but if chosen, authors should provide titles for *all* eligible references. If article titles remain missing from eligible references, the

production team will remove the existing titles at final proof stage.

## ORCIDs

Please follow any ORCID links ( after the authors' names and verify that they point to the appropriate record for each author.

## Funding Information

Information about an article's funding sources is now submitted to Crossref to help you comply with current or future funding agency mandates. Crossref's Open Funder Registry (<https://www.crossref.org/services/funder-registry/>) is the definitive registry of funding agencies. Please ensure that your acknowledgments include all sources of funding for your article following any requirements of your funding sources. Where possible, please include grant and award ids. Please carefully check the following funder information we have already extracted from your article and ensure its accuracy and completeness:

- National Science Foundation, FundRef ID <http://dx.doi.org/10.13039/100000001> (United States/US)
- Albert Einstein Institute
- H2020 Marie Skłodowska-Curie Actions, FundRef ID <http://dx.doi.org/10.13039/100010665> (Kingdom of Belgium/BE)
- H2020 European Research Council, FundRef ID <http://dx.doi.org/10.13039/100010663> (Kingdom of Belgium/BE)
- Ministero dell'Istruzione, dell'Università e della Ricerca, FundRef ID <http://dx.doi.org/10.13039/501100003407> (Repubblica Italiana/IT)

## Other Items to Check

- Please note that the original manuscript has been converted to XML prior to the creation of the PDF proof, as described above. Please carefully check all key elements of the paper, particularly the equations and tabular data.
- Title: Please check; be mindful that the title may have been changed during the peer-review process.
- Author list: Please make sure all authors are presented, in the appropriate order, and that all names are spelled correctly.
- Please make sure you have inserted a byline footnote containing the email address for the corresponding author, if desired. Please note that this is not inserted automatically by this journal.
- Affiliations: Please check to be sure the institution names are spelled correctly and attributed to the appropriate author(s).
- Receipt date: Please confirm accuracy.
- Acknowledgments: Please be sure to appropriately acknowledge all funding sources.
- References: Please check to ensure that titles are given as appropriate.
- Hyphenation: Please note hyphens may have been inserted in word pairs that function as adjectives when they occur before a noun, as in "x-ray diffraction," "4-mm-long gas cell," and "*R*-matrix theory." However, hyphens are deleted from word pairs when they are not used as adjectives before nouns, as in "emission by x rays," "was 4 mm in length," and "the *R* matrix is tested."

Note also that Physical Review follows U.S. English guidelines in that hyphens are not used after prefixes or before suffixes: superresolution, quasiequilibrium, nanoprecipitates, resonancelike, clockwise.

- Please check that your figures are accurate and sized properly. Make sure all labeling is sufficiently legible. Figure quality in this proof is representative of the quality to be used in the online journal. To achieve manageable file size for online delivery, some compression and downsampling of figures may have occurred. Fine details may have become somewhat fuzzy, especially in color figures. The print journal uses files of higher resolution and therefore details may be sharper in print. Figures to be published in color online will appear in color on these proofs if viewed on a color monitor or printed on a color printer.

- Overall, please proofread the entire *formatted* article very carefully. The redlined PDF should be used as a guide to see changes that were made during copyediting. However, note that some changes to math and/or layout may not be indicated.

## **Ways to Respond**

- **Web:** If you accessed this proof online, follow the instructions on the web page to submit corrections.
- **Email:** Send corrections to [aps-robot@luminad.com](mailto:aps-robot@luminad.com). Include the accession code DD12983 in the subject line.
- **Fax:** Return this proof with corrections to +1.855.808.3897.

## **If You Need to Call Us**

You may leave a voicemail message at +1.855.808.3897. Please reference the accession code and the first author of your article in your voicemail message. We will respond to you via email.

1  
2  
3

# Constraints on quasinormal-mode frequencies with LIGO-Virgo binary–black-hole observations

4 Abhirup Ghosh<sup>1</sup>, Richard Brito<sup>2</sup>, and Alessandra Buonanno<sup>1,3</sup>5 <sup>1</sup>*Max Planck Institute for Gravitational Physics (Albert Einstein Institute),  
Am Mühlenberg 1, Potsdam 14476, Germany*6 <sup>2</sup>*Dipartimento di Fisica, “Sapienza” Università di Roma and Sezione INFN Roma1,  
Piazzale Aldo Moro 5, 00185 Roma, Italy*7 <sup>3</sup>*Department of Physics, University of Maryland, College Park, Maryland 20742, USA*

8 (Received 23 April 2021; accepted 25 May 2021)

9 10

The no-hair conjecture in general relativity (GR) states that the properties of an astrophysical Kerr black hole (BH) are completely described by its mass and spin. As a consequence, the complex quasinormal-mode (QNM) frequencies of a binary–black-hole (BBH) ringdown can be uniquely determined by the mass and spin of the remnant object. Conversely, measurement of the QNM frequencies could be an independent test of the no-hair conjecture. This paper extends to spinning BHs earlier work that proposed to test the no-hair conjecture by measuring the complex QNM frequencies of a BBH ringdown using parameterized inspiral-merger-ringdown waveforms in the effective-one-body formalism, thereby taking full advantage of the entire signal power and removing dependency on the predicted or estimated start time of the ringdown. Our method was used to analyze the properties of the merger remnants for BBHs observed by LIGO-Virgo in the first half of their third observing (O3a) run. After testing our method with GR and non-GR synthetic-signal injections in Gaussian noise, we analyze, for the first time, two BBHs from the first (O1) and second (O2) LIGO-Virgo observing runs and two additional BBHs from the O3a run. We then provide joint constraints with published results from the O3a run. In the most agnostic and conservative scenario, where we combine the information from different events using a hierarchical approach, we obtain, at 90% credibility, that the fractional deviations in the frequency (damping time) of the dominant QNM are  $\delta f_{220} = 0.03^{+0.10}_{-0.09}$  ( $\delta\tau_{220} = 0.10^{+0.44}_{-0.39}$ ), respectively, an improvement of a factor of  $\sim 4$  ( $\sim 2$ ) over the results obtained with our model in the LIGO-Virgo publication. The single-event most-stringent constraint to date continues to be GW150914, for which we obtain  $\delta f_{220} = 0.05^{+0.11}_{-0.07}$  and  $\delta\tau_{220} = 0.07^{+0.26}_{-0.23}$ .

29 DOI:

30

## I. INTRODUCTION

The LIGO Scientific Collaboration [1] and the Virgo Collaboration [2] have recently announced their catalog of gravitational-wave (GW) signals from the first half of the third observing run (O3a) [3]. Combined with the first and second observing-run catalogs [4], the Advanced LIGO detectors at Hanford, Washington and Livingston, Louisiana [5] and the Advanced Virgo detector in Cascina, Italy [6] have now detected 50 GW events from the merger of compact objects like neutron stars and/or black holes (BHs). Alongside independent claims of detections [7–10], these results have firmly established the field of GW astronomy, five years after the first detection of a GW passing through Earth, GW150914 [11].

The observation of GWs has had significant astrophysical and cosmological implications [12–15]. It has also allowed us to probe fundamental physics and test predictions of Einstein’s theory of general relativity (GR) in the previously unexplored highly dynamical and strong field regime [16–19]. In GR, a binary–black-hole (BBH) system

is described by three distinct phases: an early *inspiral* [20], where the two compact objects spiral in, losing energy because of the emission of GWs, a *merger* [21–23] marked by the formation of a common apparent horizon, and a *ringdown* [24–28], during which the newly formed remnant object settles down to a Kerr BH emitting quasinormal modes (QNMs) (i.e., damped oscillations with specific, discrete frequencies and decay times).

The no-hair conjecture in GR [29–33] states that an (electrically neutral) astrophysical BH is completely described by two observables: mass and spin. One consequence of the no-hair conjecture is that the (complex) QNM frequencies of gravitational radiation emitted by a perturbed isolated BH are uniquely determined by its mass and spin. Hence, a test of the no-hair conjecture would involve checking for consistency between estimates of mass and spin of the remnant object across multiple QNM frequencies [34,35]. Consistency of the late-time waveform with a single QNM is a test of the ringdown of a BBH coalescence but not necessarily a test of the no-hair conjecture, which

50  
51  
52  
53  
54  
55  
56  
57  
58  
59  
60  
61  
62  
63  
64  
65  
66  
67  
68  
69

requires the measurement of (at least) two QNMs (BH spectroscopy) and consistency between them [34,36–43]. An inconsistency would indicate either a non-BH nature of the remnant object or an incompleteness of GR as the underlying theory of gravity.

The LIGO-Virgo Collaborations have released companion papers detailing their results of tests of GR for GW150914 [16] and for several GW events of the two transient catalogs (TCs): GWTC-1 [4,18] and GWTC-2 [3,19]. The results include tests of GW generation and source dynamics, where bounds are placed on parameterized deviations in the post-Newtonian (PN) coefficients describing the early inspiral, and phenomenological coefficients describing the intermediate (plunge) and merger regimes of coalescence [17,44–46]; tests of GW propagation, which assume a generalized dispersion relation and place upper bounds on the Compton wavelength and, consequently, the mass of the graviton [47,48]; and tests of the polarization of gravitational radiation using a multi-GW-detector network [49,50]. The GWTC-1 and -2 papers also check for consistency between different portions of the signal using estimates for the predicted mass and spin of the remnant object [16,51,52] and consistency of the residuals with detector noise [18,53]. None of these tests report any departure from the predictions of GR.

The first paper on tests of GR by the LIGO Collaboration [16] also provided us with the first measurement of the dominant damped-oscillation signal in the ringdown stage of a BBH coalescence, and, more recently, a similar measurement was made with the high-mass event GW190521 [54,55]. The set of available measurements was greatly expanded in the latest LIGO-Virgo O3a testing GR paper [19], where a comprehensive analysis of the properties of the remnant object, including the ringdown stage, was reported for tens of GW events. The consistency between the postmerger signal and the least-damped QNM was first demonstrated in Ref. [16] for GW150914 and confirmed through several independent analyses [40,56–58]. This was later extended to include overtones in Refs. [19,40,59]. The nature of the remnant object has also been explored through tests of BH thermodynamics, including the Hawking area theorem [60,61], the Bekenstein-Hod universal bound [62], the BH area quantization [63,64], and the consistency of the merger frequency with predictions from numerical-relativity (NR) simulations [39], or through search for echoes in the postmerger signal [65–70]. None of these tests have found evidence for non-BH nature of the remnant object (as described in GR) in LIGO-Virgo BBH observations.

With current ground-based detectors, only a small fraction of BBH coalescences lead to a detectable postmerger GW signal, and, even for these events, the signal-to-noise ratio (SNR) in the postmerger signal is, in most cases, only slightly above threshold for detection [18,19]. This is particularly important, given that most of the tests mentioned above restrict the data to this postmerger signal

which, while being agnostic to deviations in the premerger dynamics, significantly reduces parameter-estimation capabilities. Added to a lack of SNR is the ambiguity in clearly defining a start time for the ringdown phase (discussed, for example, in Refs. [71–73]). Defining such a time is particularly important in order to avoid possible systematic errors that may occur if one tries to extract the fundamental QNMs too early after merger, since the higher-order overtones dominate the ringdown signal closer to merger [59,74]. In some tests [39,57], the ringdown start time has been left as a free parameter to be estimated directly from the data, whereas, in other cases, the ringdown start time is predicted from corresponding full-signal parameter-estimation analyses (see `pyRing` analysis in Ref. [19]). Uncertainties in estimates of the ringdown start time, as well as an overall lack of SNR in the postmerger signal, given typical sensitivities of ground-based detectors, can result in significant statistical uncertainties in the measurement of some of the QNM properties. This is especially true for the measurement of the QNM damping times, which are, in general, harder to measure from the data. Hence, one might want to look at alternate methods to measure QNMs using information from as much of the signal as possible.

An independent approach to BH spectroscopy, based on the full-signal analysis, was introduced in Ref. [56] (henceforth referred to as paper I). Unlike methods that focus only on the postmerger signal, it employs the complete inspiral-merger-ringdown (IMR) waveform to measure the complex QNM frequencies. In the current version, this method assumes that GR provides a very good description of the signal up to merger while being agnostic about the complex QNM frequencies. This allows one to access the full SNR of the signal, reducing measurement uncertainties. However, we note that this method can incorporate deviations from GR, notably from the (known) PN coefficients, also during the long inspiral stage [17–19], and can, in principle, incorporate deviations from GR, notably from the parameters calibrated to NR simulations, in the late inspiral and plunge. Moreover, in this method, the definition of the ringdown start time is built into the merger-ringdown model and does not need to be either left as an additional free parameter or fixed using alternate definitions. While paper I presented the method and tested it for nonspinning BBHs, here we extend the analysis to the more realistic astrophysical case in which BHs carry spin. Furthermore, the IMR waveform model used in this paper is more accurate than that employed in paper I, because it contains higher-order corrections in PN theory and it was calibrated to a much larger set of NR waveforms [75]. All astrophysical BHs are expected to be spinning, and ignoring effects of spin has been shown to introduce systematic biases in the measurement of the source properties.

The rest of the paper is organized as follows. Section II A describes our parameterized IMR waveform model.

In Sec. II B, we define our framework to test GR, notably how we can measure complex QNM frequencies with our parameterized model within a Bayesian formalism, and validate it using several synthetic-signal injection studies in Gaussian noise in Sec. III. Then, in Sec. IV, we apply our method on real GW events in LIGO and Virgo data. In particular, we analyze the GWTC-2 events and obtain the most stringent constraints on the dominant (complex) QNM frequencies. Finally, in Sec. V, we provide a summary of our results and discuss future developments.

## II. WAVEFORM MODEL AND STATISTICAL STRATEGY TO MEASURE QUASINORMAL MODES

A GW signal from the (quasicircular) coalescence of two BHs is completely described in GR by 15 parameters,  $\xi_{\text{GR}}$ . These can be grouped into the *intrinsic* parameters—the (source) masses  $m_1$  and  $m_2$  and spins  $\vec{S}_1$  and  $\vec{S}_2$  of the component objects in the binary—and the *extrinsic* parameters—a reference time  $t_c$  and phase  $\phi_c$ , the sky position of the binary ( $\alpha, \delta$ ), the luminosity distance  $d_L$ , and the binary’s orientation described through the inclination of the binary  $i$  and its polarization  $\psi$ . We also introduce the total (source) mass  $M = m_1 + m_2$  and the (dimensionless) symmetric mass ratio  $\nu = m_1 m_2 / M^2$ . We also follow the convention  $m_1 > m_2$  and, hence, the asymmetric mass ratio  $q = m_1 / m_2 \geq 1$ . We also introduce the detector masses  $m_{1\text{det}} = (1+z)m_1$  and  $m_{2\text{det}} = (1+z)m_2$ , where  $z$  is the redshift.

Here, we focus on BHs with spins aligned or antialigned with the orbital angular momentum (henceforth, aligned spin). In this case, the GW signal depends on 11 parameters. We denote the aligned-spin (dimensionless) components as  $\chi_i = |\vec{S}_i|/m_i^2$ , where  $i = 1, 2$  for the two BHs.

### A. Parameterized waveform model

As in paper I, we use an IMR waveform model developed within the effective-one-body (EOB) formalism [76,77]. However, whereas paper I was limited to non-spinning multipolar waveforms, here we use as our baseline model the aligned-spin multipolar waveform model developed in Ref. [78]. In addition to being calibrated to NR simulations, this model also uses information from BH perturbation theory for the merger and ringdown phases. Henceforth, we will denote this model by SEOBNR for short.<sup>1</sup>

In the observer’s frame, the GW polarizations can be written as

$$h_+(\iota, \varphi_0; t) - i h_\times(\iota, \varphi_0; t) = \sum_{\ell, m} {}_{-2}Y_{\ell m}(\iota, \varphi_0) h_{\ell m}(t), \quad (2.1)$$

<sup>1</sup>In the LIGO Algorithm Library (LAL), this waveform model is called SEOBNRv4HM.

where  $\varphi_0$  is the azimuthal direction to the observer (note that without loss of generality we can take  $\phi_c \equiv \varphi_0$ ) while  ${}_{-2}Y_{\ell m}(\iota, \varphi_0)$  are the  $-2$  spin-weighted spherical harmonics, where  $(\ell, m)$  are the usual indices that describe the angular dependence of the spin-weighted spherical harmonics, with  $\ell \geq 2$ ,  $-\ell \leq m \leq \ell$ . The SEOBNR model we employ includes the  $(\ell, |m|) = (2, 2), (2, 1), (3, 3), (4, 4)$ , and  $(5, 5)$  modes [78]. For each  $(\ell, m)$ , the inspiral-plunge-merger-ringdown SEOBNR waveform is schematically given by

$$h_{\ell m}(t) = h_{\ell m}^{\text{insp-plunge}} \theta(t_{\text{match}}^{\ell m} - t) + h_{\ell m}^{\text{merger-RD}} \theta(t - t_{\text{match}}^{\ell m}), \quad (2.2)$$

where  $\theta(t)$  is the Heaviside step function and  $h_{\ell m}^{\text{insp-plunge}}$  represents the inspiral-plunge part of the waveform, whereas  $h_{\ell m}^{\text{merger-RD}}$  denotes the merger-ringdown waveform, which reads [75,78]

$$h_{\ell m}^{\text{merger-RD}}(t) = \nu \tilde{A}_{\ell m}(t) e^{i\tilde{\phi}_{\ell m}(t)} e^{-i\sigma_{\ell m 0}(t-t_{\text{match}}^{\ell m})}, \quad (2.3)$$

where  $\nu$  is the symmetric mass ratio of the binary and  $\sigma_{\ell m 0} = 2\pi f_{\ell m 0} - i/\tau_{\ell m 0}$  denotes the complex frequency of the fundamental QNMs of the remnant BH, i.e., QNMs with overtone index  $n = 0$ . We denote the oscillation frequencies by  $f_{\ell m 0} \equiv \text{Re}(\sigma_{\ell m 0})/(2\pi)$  and the decay times by  $\tau_{\ell m 0} \equiv -1/\text{Im}(\sigma_{\ell m 0})$ . The functions  $\tilde{A}_{\ell m}(t)$  and  $\tilde{\phi}_{\ell m}(t)$  are given by [75,78]

$$\tilde{A}_{\ell m}(t) = c_{1,c}^{\ell m} \tanh[c_{1,f}^{\ell m}(t - t_{\text{match}}^{\ell m}) + c_{2,f}^{\ell m}] + c_{2,c}^{\ell m}, \quad (2.4a)$$

$$\tilde{\phi}_{\ell m}(t) = \phi_{\text{match}}^{\ell m} - d_{1,c}^{\ell m} \log \left[ \frac{1 + d_{2,f}^{\ell m} e^{-d_{1,f}^{\ell m}(t-t_{\text{match}}^{\ell m})}}{1 + d_{2,f}^{\ell m}} \right], \quad (2.4b)$$

respectively, where  $\phi_{\text{match}}^{\ell m}$  is the phase of the inspiral-plunge mode  $(\ell, m)$  computed at  $t = t_{\text{match}}^{\ell m}$ . The coefficients  $d_{1,c}^{\ell m}$  and  $c_{i,c}^{\ell m}$  with  $i = 1, 2$  are fixed by imposing that the functions  $\tilde{A}_{\ell m}(t)$  and  $\tilde{\phi}_{\ell m}(t)$  are of class  $C^1$  at  $t = t_{\text{match}}^{\ell m}$ , when matching the merger-ringdown waveform to the inspiral-plunge SEOBNR waveform  $h_{\ell m}^{\text{inspiral-plunge}}(t)$ . This allows us to write the coefficients  $c_{i,c}^{\ell m}$  as [78]

$$c_{1,c}^{\ell m} = \frac{1}{c_{1,f}^{\ell m} \nu} [\partial_t |h_{\ell m}^{\text{insp-plunge}}(t_{\text{match}}^{\ell m})| - \sigma_{\ell m}^{\text{R}} |h_{\ell m}^{\text{insp-plunge}}(t_{\text{match}}^{\ell m})|] \cosh^2(c_{2,f}^{\ell m}), \quad (2.5a)$$

$$c_{2,c}^{\ell m} = -\frac{|h_{\ell m}^{\text{insp-plunge}}(t_{\text{match}}^{\ell m})|}{\nu} + \frac{1}{c_{1,f}^{\ell m} \nu} [\partial_t |h_{\ell m}^{\text{insp-plunge}}(t_{\text{match}}^{\ell m})| - \sigma_{\ell m}^{\text{R}} |h_{\ell m}^{\text{insp-plunge}}(t_{\text{match}}^{\ell m})|] \cosh(c_{2,f}^{\ell m}) \sinh(c_{2,f}^{\ell m}) \quad (2.5b)$$

259 and  $d_{1,c}^{\ell m}$  as

$$d_{1,c}^{\ell m} = [\omega_{\ell m}^{\text{insp-plunge}}(t_{\text{match}}) - \sigma_{\ell m}^I] \frac{1 + d_{2,f}^{\ell m}}{d_{1,f}^{\ell m} d_{2,f}^{\ell m}}, \quad (2.6)$$

260 where we denoted  $\sigma_{\ell m}^R \equiv \text{Im}(\sigma_{\ell m 0}) < 0$  and  $\sigma_{\ell m}^I \equiv$   
262  $-\text{Re}(\sigma_{\ell m 0})$  and  $\omega_{\ell m}^{\text{insp-plunge}}(t)$  is the frequency of the  
263 inspiral-plunge EOB mode. The coefficients  $c_{i,f}^{\ell m}$  and  
264  $d_{i,f}^{\ell m}$  are obtained through fits to NR and Teukolsky-  
265 equation-based waveforms and can be found in the  
266 Appendix C of Ref. [78].

267 In the SEOBNR model constructed in Ref. [78], the  
268 complex frequencies  $\sigma_{\ell m 0}$  are expressed in terms of the  
269 final BH mass and spin [35,79], and the latter are related to  
270 the BBH's component masses and spins through NR-fitting  
271 formulas obtained in GR [80,81]. Here, instead, in the spirit  
272 of what was done in paper I, we promote the QNM  
273 (complex) frequencies to be free parameters of the model  
274 while keeping the inspiral-plunge modes  $h_{\ell m}^{\text{inspiral-plunge}}(t)$   
275 fixed to their GR values. More explicitly, we introduce a  
276 parameterized version of the SEOBNR model where the  
277 frequency and the damping time of the  $\ell m 0$  mode [i.e.,  
278  $(f_{\ell m 0}$  and  $\tau_{\ell m 0})$ ] are defined through the fractional deviations  
279 ( $\delta f_{\ell m 0}$  and  $\delta \tau_{\ell m 0}$ ) from the corresponding GR  
280 values [36,37].

281 Thus,

$$f_{\ell m 0} = f_{\ell m 0}^{\text{GR}}(1 + \delta f_{\ell m 0}), \quad (2.7a)$$

$$\tau_{\ell m 0} = \tau_{\ell m 0}^{\text{GR}}(1 + \delta \tau_{\ell m 0}). \quad (2.7b)$$

283 The GR quantities ( $f_{\ell m 0}^{\text{GR}}$  and  $\tau_{\ell m 0}^{\text{GR}}$ ) are constructed using  
284 the NR-fitting formula from Refs. [80,81] and are functions  
285 of the initial masses and spins ( $m_1$ ,  $m_2$ ,  $\chi_1$ , and  $\chi_2$ ). Hence,

$$f_{\ell m 0} = f_{\ell m 0}(m_1, m_2, \chi_1, \chi_2, \delta f_{\ell m 0}, \delta \tau_{\ell m 0}), \quad (2.8a)$$

$$\tau_{\ell m 0} = \tau_{\ell m 0}(m_1, m_2, \chi_1, \chi_2, \delta f_{\ell m 0}, \delta \tau_{\ell m 0}). \quad (2.8b)$$

286 We denote such a parameterized waveform model  
287 pSEOBNR.<sup>2</sup> We note that, when leaving  $\sigma_{\ell m}$  to vary  
288 freely, the functions  $\tilde{A}_{\ell m}(t)$  and  $\tilde{\phi}_{\ell m}(t)$ , in general, also  
289 differ from the GR predictions, since those functions  
290 depend on the QNM complex frequencies, as can be seen  
291 from the expressions for  $c_{i,c}^{\ell m}$  and  $d_{i,c}^{\ell m}$  in Eqs. (2.5a), (2.5b),  
292 and (2.6). As a consequence, the ringdown signal (ampli-  
293 tude and phase) soon after merger deviates from the one  
294 predicted by GR.

<sup>2</sup>This waveform model is called pSEOBNRv4HM in LAL.

## B. Bayesian parameter-estimation technique

296

The parameterized model pSEOBNR described above  
introduces an additional set of non-GR parameters,  
 $\xi_{\text{nGR}} = (\delta f_{\ell m 0}, \delta \tau_{\ell m 0})$ , corresponding to each  $(\ell, m)$   
QNM present in the GR waveform model SEOBNR. One  
then proceeds to use the Bayes theorem to obtain  
the *posterior* probability distribution on  $\lambda = \{\xi_{\text{GR}}, \xi_{\text{nGR}}\}$ ,  
given a hypothesis  $\mathcal{H}$ :

$$P(\lambda|d, \mathcal{H}) = \frac{P(\lambda|\mathcal{H})\mathcal{L}(d|\lambda, \mathcal{H})}{P(d|\mathcal{H})}, \quad (2.9)$$

where  $P(\lambda|\mathcal{H})$  is the *prior* probability distribution  
and  $\mathcal{L}(d|\lambda, \mathcal{H})$  is called the *likelihood* function. The  
denominator is a normalization constant  $P(d|\mathcal{H}) = \int P(\lambda|\mathcal{H})\mathcal{L}(d|\lambda, \mathcal{H})d\lambda$ , called the marginal likelihood, or  
the *evidence* of the hypothesis  $\mathcal{H}$ . In this case, our  
hypothesis  $\mathcal{H}$  is that the data contain a GW signal that  
is described by the pSEOBNR waveform model  $h(\lambda)$  and  
stationary Gaussian noise described by a power spectral  
density (PSD)  $S_n(f)$ . The likelihood function can con-  
sequently be defined as

$$\mathcal{L}(d|\lambda, \mathcal{H}) \propto \exp\left[-\frac{1}{2}\langle d - h(\lambda)|d - h(\lambda)\rangle\right], \quad (2.10)$$

where  $\langle . | . \rangle$  is the usual noise-weighted inner product:

$$\langle A|B \rangle = \int_{f_{\text{low}}}^{f_{\text{high}}} df \frac{\tilde{A}^*(f)\tilde{B}(f) + \tilde{A}(f)\tilde{B}^*(f)}{S_n(f)}. \quad (2.11)$$

The quantity  $\tilde{A}(f)$  denotes the Fourier transform of  $A(t)$ ,  
and the \* indicates complex conjugation. The limits of  
integration  $f_{\text{low}}$  and  $f_{\text{high}}$  define the bandwidth of the  
sensitivity of the GW detector. We usually assume  $f_{\text{high}}$  to  
be the Nyquist frequency, whereas  $f_{\text{low}}$  is dictated by the  
performance of the GW detector at low frequency. Here, we  
follow the choice made in the LIGO-Virgo analysis [34].  
Namely, for all events and injections we consider, we set  
 $f_{\text{low}} = 20$  Hz, except for the GW190521-like injection and  
the real GW190521 event, for which we set  $f_{\text{low}} = 11$  Hz  
[54,55]. Owing to the large dimensionality of the parameter  
set  $\lambda$ , the posterior distribution  $P(\lambda|d, \mathcal{H})$  in Eq. (2.9) is  
computed by stochastically sampling the parameter space  
using techniques such as Markov-chain Monte Carlo  
(MCMC) [82,83] or nested sampling [84]. For this paper,  
we use the LALInference [85] and Bilby codes [86–88] that  
provide an implementation of the parallelly tempered  
MCMC and nested sampling algorithms, respectively, for  
computing the posterior distributions.

Given the full-dimensional posterior probability density  
function  $P(\lambda|d, \mathcal{H})$ , we can marginalize over the *nuisance*  
parameters, to obtain the marginalized posterior probability  
density function over the QNM parameters  $\xi_{\text{nGR}}$ :

TABLE I. Parameters of the synthetic-signal injections, chosen to be similar to the actual GW events indicated in the first column (first two rows). The parameters ( $m_{1\text{det}}$  and  $m_{2\text{det}}$ ) are the detector-frame masses of the primary and secondary BHs, respectively. The third row indicates the parameters of the SXS BBH waveform used in Sec. III C. The second column refers to the detector network used, with H, L, and V referring to LIGO-Hanford, LIGO-Livingston, and Virgo, respectively. The quantities  $\rho_{\text{IMR}}$ ,  $\rho_{\text{insp}}$ , and  $\rho_{\text{postinsp}}$  are the SNR of the full IMR signal, SNR up to a certain cutoff frequency, and SNR after the cutoff frequency, respectively. In each case, the cutoff frequency is assumed to be the frequency at the innermost circular stable orbit corresponding to the remnant Kerr BH.

Injection	Network	$m_{1\text{det}} (M_\odot)$	$m_{2\text{det}} (M_\odot)$	$\chi_1$	$\chi_2$	$\rho_{\text{IMR}}$	$\rho_{\text{insp}}$	$\rho_{\text{postinsp}}$
GW150914-like	HL	39	31	0.0	0.0	25	22	12
GW190521-like	HL	150	120	0.02	-0.39	20	8	18
SXS:BBH:0166	HLV	72	12	0.0	0.0	71	58	41

$$P(\xi_{\text{nGR}}|d, \mathcal{H}) = \int P(\lambda|d, \mathcal{H}) d\xi_{\text{GR}}. \quad (2.12)$$

For most of the results discussed in this paper, we restrict ourselves to the  $(\ell m) = (2, 2)$  and/or  $(3, 3)$  modes. In those cases, we assume  $\xi_{\text{nGR}} = \{\delta f_{220}, \delta \tau_{220}\}$  and/or  $\{\delta f_{330}, \delta \tau_{330}\}$  and fix all the other  $(\ell m)$  modes to their GR predictions (i.e.,  $\delta f_{\ell m0} = \delta \tau_{\ell m0} = 0$ ). This is because, for most of the high-mass BH events that we find most appropriate for this test, the LIGO-Virgo observations are consistent with nearly-equal-mass face-on and -off BBHs, for which power in the subdominant modes is not enough to attempt to measure more than one QNM complex frequency.

Lastly, throughout our analysis, we assume uniform priors on our non-GR QNM parameters ( $\delta f_{\ell m0}$  and  $\delta \tau_{\ell m0}$ ). We note that, since the priors on  $(f_{\ell m0}^{\text{GR}}, \tau_{\ell m0}^{\text{GR}})$  are derived through NR fits, from the corresponding priors on the initial masses and spins, this leads to a nontrivial prior on the final reconstructed frequency and damping time,  $(f_{\ell m0}, \tau_{\ell m0})$ . Also, given the definition of the damping time in Sec. II A, we note that  $\delta \tau_{\ell m0} = -1$  leads to the imaginary part of the QNM complex frequency going to infinity. We avoid this by restricting the minimum of the prior on  $\delta \tau_{\ell m0}$  to be greater than  $-1$ .

### III. SYNTHETIC-SIGNAL INJECTION STUDY

#### A. Simulations using GR signals in Gaussian noise

We now demonstrate our method using synthetic-signal injections describing GWs from BBHs in GR. We employ colored Gaussian noise with PSDs for LIGO and Virgo detectors during the fourth observing (O4) run [89], which is expected to start in the second half of 2022 [6,90]. For the mock BBH signals, we choose parameters similar to two specific GW events, GW150914 [11] and GW190521 [54]. We list them in Table I. These two binary systems are representative of the kind of systems for which the QNM measurement is most suitable, notably high-mass BBH events which are loud enough that the pre- and postmerger SNRs return reliable parameter-estimation results.

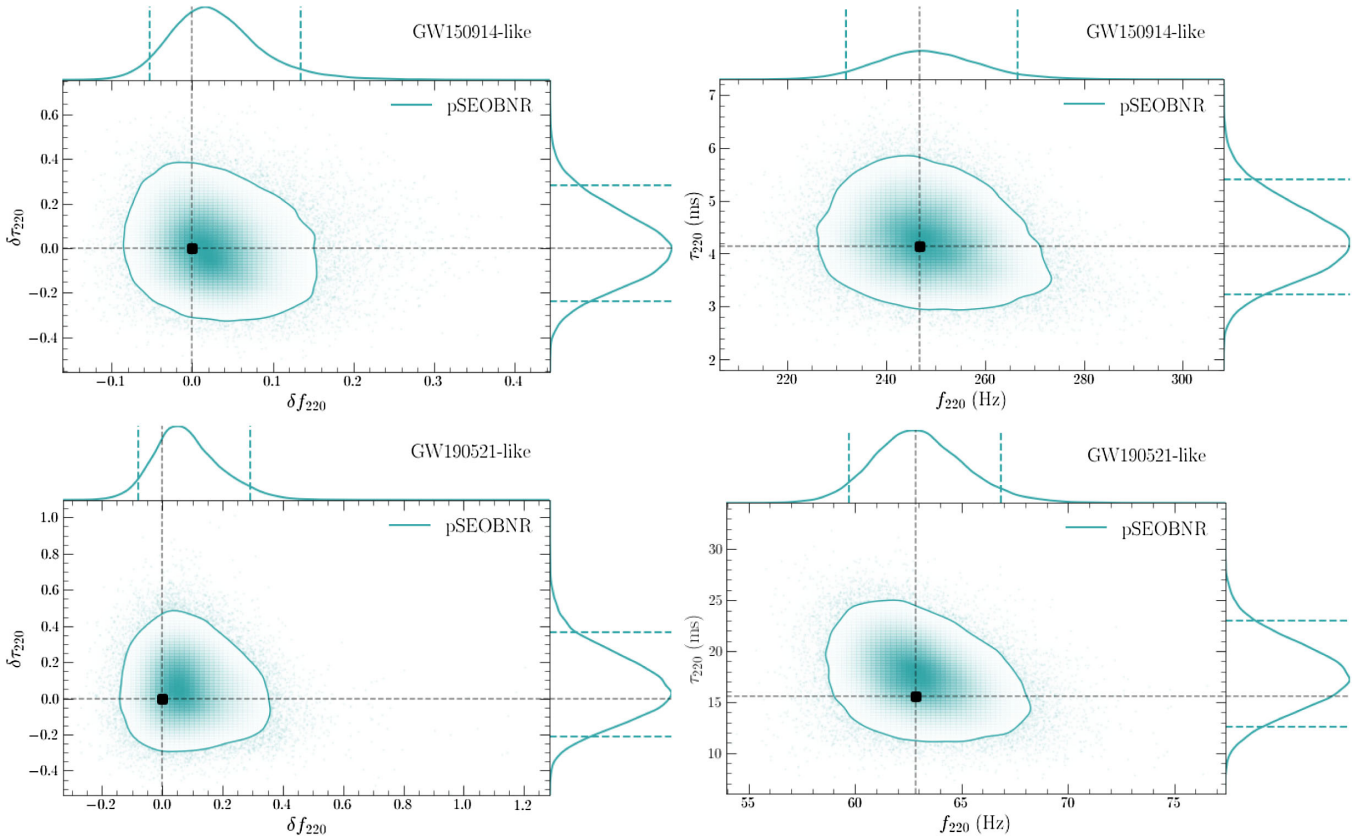
To avoid possible systematic biases in our parameter-estimation analysis due to error in waveform modeling, we use the GR version of the same waveform, SEOBNR (i.e., without allowing for deviations in the QNM parameters), to simulate our GW signal. And, to avoid systematic biases due to noise, we use an averaged (zero-noise) realization of the noise.<sup>3</sup> Since nearly-equal-mass binaries like GW150914 and GW190521 observed at moderately high SNRs are not expected to have a loud ringdown signal, we restrict ourselves to estimating the frequency and damping time of only one QNM  $(\ell m) = (2, 2)$  (i.e.,  $\{\delta f_{220}, \delta \tau_{220}\}$ ) while fixing the other QNM frequencies to their GR values.

We find, as one might expect, that the posterior distributions on the parameters describing fractional deviations in the frequency and damping time are consistent with zero (left panels in Fig. 1). One can then convert these fractional quantities into absolute quantities using the relations given in Eqs. (2.7a) and (2.7b) and construct posterior distributions on these effective quantities,  $(f_{220}$  and  $\tau_{220})$  (right panels in Fig. 1). In each of these cases, the recovered two-dimensional posteriors are consistent with the GR predictions (black dashed lines).

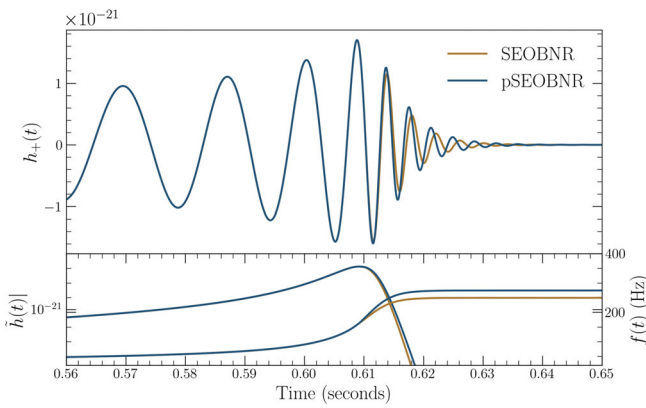
#### B. Simulations using non-GR signals in Gaussian noise

To demonstrate the robustness of the method in detecting possible deviations from GR, we inject synthetic GW signals which are identical to the corresponding GR prediction up to merger and differ in their postmerger description. We again choose binary parameters similar to GW150914 and GW190521 (see Table I) but set  $\delta f_{220} = \delta \tau_{220} = 0.1$ . In other words, we assume that the frequency and damping time of our non-GR signal is 10% more than the corresponding GR prediction, although the premerger signal is identical to GR. In Fig. 2, we show this non-GR waveform, pSEOBNR, with respect to the original GR template, SEOBNR. We see that the waveforms are identical in amplitude and instantaneous frequency up to

<sup>3</sup>A detailed study on noise systematics for one of the GW events is presented in Appendix A.



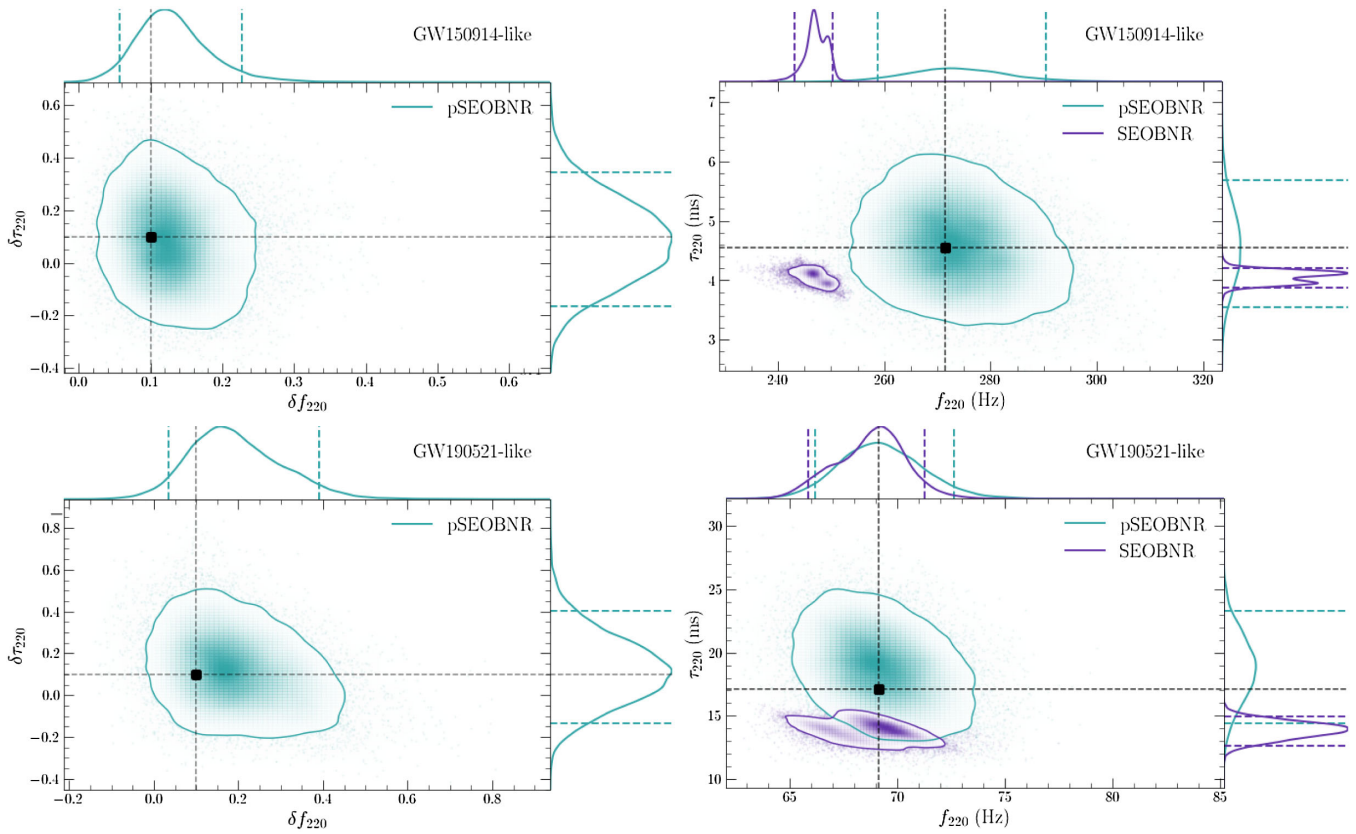
F1:1 FIG. 1. Posterior probability distribution on the fractional deviations in the frequency and damping time of the (2,2) QNM ( $\delta f_{220}$  and  
F1:2  $\delta\tau_{220}$ ) (left panels) and the reconstructed quantities ( $f_{220}$  and  $\tau_{220}$ ) (right panels) for GR injections (SEOBNR)  
F1:3 with initial parameters similar to GW150914 (top panels) and GW190521 (bottom panels) (see Table I). The 2D contour marks the 90% credible region,  
F1:4 while the dashed lines on the 1D marginalized distributions mark the 90% credible levels. The black vertical and horizontal lines mark the  
F1:5 injection values.



F2:1 FIG. 2. Top panel: the + polarization of the gravitational  
F2:2 waveform  $h_+(t)$  from a GW150914-like event where the post-  
F2:3 merger is described by GR (i.e.,  $\delta f_{220} = \delta\tau_{220} = 0$ ) and where  
F2:4 the merger ringdown is modified (i.e.,  $\delta f_{220} = \delta\tau_{220} = 0.1$ ).  
F2:5 Bottom panel: comparison of the evolution of the amplitude,  
F2:6  $|h(t)|$  (left), and instantaneous frequency  $f(t)$  (right) for the GR  
F2:7 and non-GR signal.

the merger (lower panel), beyond which the red curve (GR template) and blue curve (non-GR template) differ. We summarize the results of the Bayesian analysis in Fig. 3, where we show the posterior probability distributions for  $(\delta f_{220}, \delta\tau_{220})$  or, equivalently,  $(f_{220}, \tau_{220})$ . We find that they are consistent with the corresponding values of the injection parameters, indicated by the black dashed lines. We also note that at the SNRs we consider, since statistical uncertainties dominate systematic biases, the measurement excludes, at the 90% credible level, the GR prediction of the frequency ( $\delta f_{220} = 0$ ) but includes the prediction of the damping time ( $\delta\tau_{220} = 0$ ). However, with louder events, one would expect these measurement errors to shrink and the  $\tau_{220}$  measurement to be inconsistent with the GR prediction, as well.

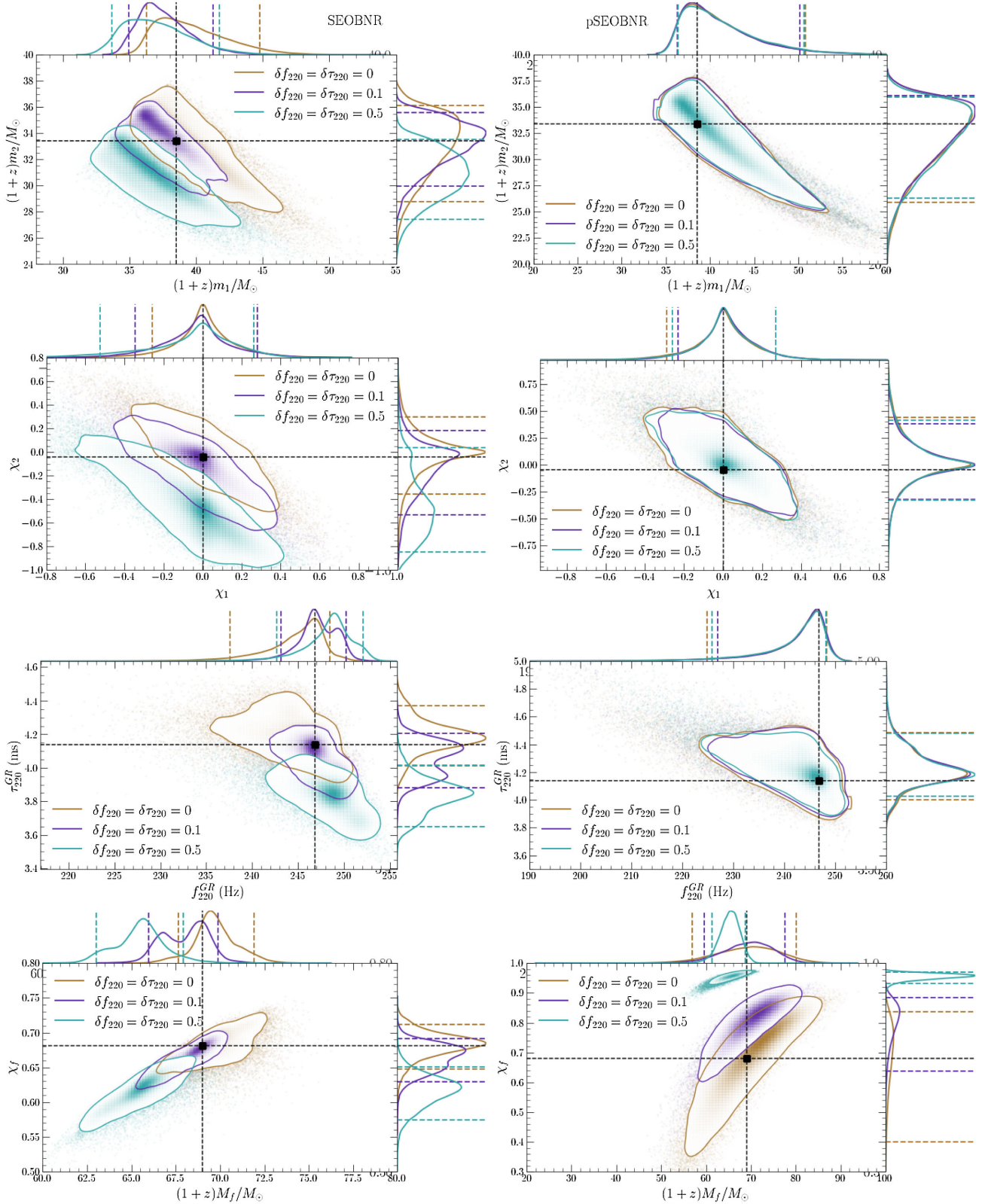
We additionally investigate the effects of erroneously assuming that an underlying non-GR signal can be well described by a GR one. We do this by estimating the parameters of our non-GR signals using the GR waveform model SEOBNR instead of the parameterized pSEOBNR. The resulting one- and two-dimensional posteriors are



F3:1 FIG. 3. Posterior probability distribution on the fractional deviations in the frequency and damping time of the (2,2) QNM ( $\delta f_{220}$  and  
F3:2  $\delta \tau_{220}$ ) (left panels) and the reconstructed quantities ( $f_{220}$  and  $\tau_{220}$ ) (right panels) for non-GR injections (pSEOBNR) with parameters of  
F3:3 GW150914-like (top panels) and GW190521-like (bottom panels) as given in Table I. The non-GR signal has a deviation:  
F3:4  $\delta f_{220} = \delta \tau_{220} = 0.1$ . The 2D contour marks the 90% credible region, while the dashed lines on the 1D marginalized distributions mark  
F3:5 the 90% credible levels. The black vertical and horizontal lines mark the injection values. In the right panels, we additionally show  
F3:6 measurements using a GR (SEOBNR) waveform for the GW150914-like (upper panel) and GW190521-like (lower panel) injections.  
F3:7 The measurements with SEOBNR waveforms are visibly biased.

437 shown in the right panels in Fig. 3 by purple curves for the  
438 GW150914-like (top) and GW190521-like (bottom) signals.  
439 For both signals, we find the 2D  
440 SEOBNR estimates are markedly biased with respect to  
441 the pSEOBNR estimates. We investigate this impact on the  
442 estimation of the GR parameters  $\xi_{\text{GR}}$  by changing the  
443 magnitude of deviation in the non-GR parameters more in  
444 Fig. 4. We restrict ourselves to a GW150914-like event  
445 and, for comparison, add a synthetic signal with  
446  $\delta f_{220} = \delta \tau_{220} = 0.5$ , or 50% deviation, alongside the  
447 10% non-GR signal and a signal with no deviation  
448 (essentially GR) mentioned above. The left (right) panels  
449 show the posterior probability distributions of the three  
450 signals using the GR, SEOBNR (non-GR, pSEOBNR)  
451 waveform model. The first difference we note is the  
452 SEOBNR recoveries yield biased estimates when the  
453 underlying signal is non-GR, while the pSEOBNR recoveries  
454 do not. Furthermore, as we increase the deviations,  
455 while the SEOBNR recoveries expectedly get more biased,  
456 the pSEOBNR measurements are robust in consistently  
457 recovering the injected value. This gives us confidence that

458 the pSEOBNR model can accurately measure QNM  
459 properties without biasing measurements of inspiral quan-  
460 tities, like masses and spins. As we increase the deviation,  
461 the remnant object rings down at a higher frequency and  
462 damping time. The resulting pSEOBNR signal is longer  
463 than the GR (SEOBNR) prediction. When we try to fit the  
464 SEOBNR model to this signal (left column in Fig. 4), the  
465 template tries to fit parameters appropriate for a longer  
466 signal, i.e., smaller masses and spins. Hence, with increas-  
467 ing deviations, the recovered masses and spins have a  
468 tendency to shift toward lower values. To compute the  
469 samples of the final mass and spin in the last row, we start  
470 from the samples of the complex QNM frequencies ( $f_{220}$  and  
471  $\tau_{220}$ ), which are obtained from the fractional deviation  
472 samples ( $\delta f_{220}$  and  $\delta \tau_{220}$ ) and the GR quantities ( $f_{220}^{\text{GR}}$  and  
473  $\tau_{220}^{\text{GR}}$ ) using Eqs. (2.7a) and Eq. (2.7b), and then invert them  
474 using the fitting formula in Ref. [35]. The three BBH  
475 signals,  $\delta f_{220} = \delta \tau_{220} = 0, 0.1, 0.5$ , correspond to three  
476 unique sets of values for  $(M_f, \chi_f)$ . These predicted values  
477 are correctly recovered by the pSEOBNR waveform  
478 (bottom-right plot in Fig. 4), leading to three distinct



F4:1 FIG. 4. Comparison of a GW150914-like injection's parameters when signals with zero, 10%, and 50% deviations ( $\delta f_{220} = \delta \tau_{220} = 0, 0.1, 0.5$ ) are recovered using a GR (SEOBNR) (left panels) or a non-GR (pSEOBNR) (right panels) waveform model. The panels (from top to bottom) show the 2D posteriors (with 90% credible levels) and corresponding marginalized 1D posteriors (with 90% credible levels) in (detector-frame) masses (first row), dimensionless spins (second row), GR predictions of frequency and damping time (third row), and the remnant mass and spin predictions ( $M_f$  and  $\chi_f$ ) (fourth row) from the frequency and damping time. In each case, the injection values are indicated by the black dashed lines. In the lowermost panel, the injection values of the final mass and spin correspond to the injection with no deviations. The  $\delta f_{220} = \delta \tau_{220} = 0.1$  signal is identical to the results shown in Fig. 3.

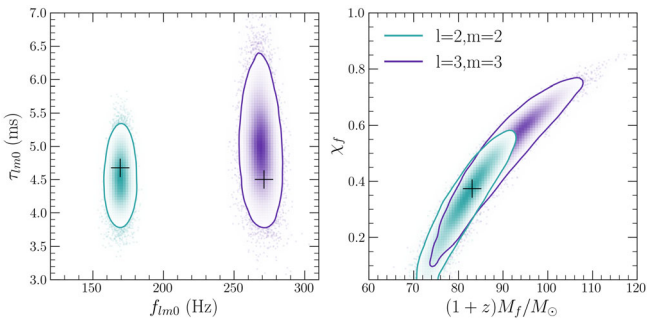
479  
480  
481  
and disjointed 2D posteriors on  $(M_f, \chi_f)$ , unlike the  
SEOBNR analysis (to reduce clutter in the plot, we just  
plot the injection values for  $\delta f_{220} = \delta \tau_{220} = 0$ ).  
482

### C. Test of the no-hair conjecture

483  
484  
485  
486  
487  
Finally, we provide a simple demonstration of a test of  
the no-hair theorem using our model. As described in the  
introduction, any test of the no-hair theorem of BHs would  
need to involve independent measurements of (at least) two  
different QNMs.  
488

489  
490  
491  
492  
493  
494  
495  
496  
497  
498  
499  
500  
501  
Here, we use an NR GW signal from the SXS catalog  
[91] corresponding to a nonspinning BBH with mass ratio  
 $q = 6$  (SXS:BBH:0166) and total mass  $M = 84 M_\odot$  (see  
Table I). We choose an asymmetric system to increase the  
SNR in the higher modes. We also choose the distance and  
orientation of the binary such that the total SNR in the  
three-detector network of LIGO Hanford, Livingston, and  
Virgo is  $\sim 70$ . Based on the LIGO-Virgo observations  
during the first three observing runs, such asymmetric  
and loud signals are no longer just a theoretical prediction  
but quite plausible during O4. Using this signal, we attempt  
to measure both the (2,2) and (3,3) QNMs. For this injected  
signal, the SNR in other subdominant modes is too low to  
be able to measure them.  
502

503  
504  
505  
506  
507  
508  
509  
510  
511  
512  
513  
We summarize our results in Fig. 5. Given the injection  
parameters, the predicted values of the (2,2) and (3,3)  
frequency and damping time are (169.45 Hz, 4.68 ms) and  
(271.21 Hz, 4.50 ms), respectively. The left panel in Fig. 5  
shows that the 2D posteriors on the (2,2) and (3,3) QNMs  
are consistent with the predictions for a BBH merger in GR,  
indicated by the black plus sign. Using fitting formulas  
provided in Ref. [35], specifically, Eqs. (2.1), (E1), and  
(E3) and Tables VIII and IX for the fitting coefficients, we  
infer the 2D posterior probability distribution on the final  
mass and spin as predicted independently by the (2,2)  
(blue) and (3,3) (red) QNMs in the right panel in Fig. 5.  
514



F5:1  
FIG. 5. Posterior probability distribution on the frequency and  
F5:2 damping time of the (2,2) and (3,3) QNM (left panel) and the final  
F5:3 mass and spin inferred from the complex frequencies (right  
F5:4 panel), when a NR signal with parameters  $q = 6$ ,  $M = 84 M_\odot$ ,  
F5:5 and  $\text{SNR} = 75$  is injected in Gaussian noise and recovered with  
F5:6 the pSEOBNR waveform model. The plus signs mark the GR  
F5:7 predictions.  
F5:8

The two independent estimates are consistent with each  
other and correspond to a unique mass and spin for the  
remnant BH ( $83.08 M_\odot$ , 0.37) indicated by the plus sign.  
As a consequence, this may be considered as a test of the  
no-hair conjecture. For most of the events observed so far,  
the power in the (3,3) has not been sufficient to measure it  
along with the (2,2). However, it might also be possible to  
combine information from multiple observations over the  
coming few years to obtain meaningful constraints on the  
(3,3) and other subdominant QNMs [36,37,92].  
514  
515  
516  
517  
518  
519  
520  
521  
522  
523

## IV. CONSTRAINTS ON QNM FREQUENCIES USING LIGO-VIRGO DATA

The LIGO-Virgo Collaboration recently released their  
testing GR catalog containing results for events observed  
during O3a [19]. For the test that we present here, the  
results shown in Ref. [19] include only events which pass a  
threshold for the median detector-frame total mass  $\geq 90 M_\odot$  and SNRs in the pre- and postmerger regions  
 $\geq 8$ .<sup>4</sup> The SNR threshold ensures that the signal contains  
sufficient information in both the inspiral and merger stages  
to break the degeneracy between the binary's total mass and  
the non-GR deviations ( $\delta f_{220}$  and  $\delta \tau_{220}$ ). Such strong  
degeneracy arises from the fact that the complex QNM  
frequencies are inversely proportional to the total mass [35]  
such that one can always obtain the same fundamental  
frequency or damping time by appropriately increasing (or  
decreasing) the total mass and the deviation parameters in  
the same direction. This degeneracy is especially important  
in low-SNR events with negligible higher modes and for  
which only the postmerger is detectable, rendering the  
measurement of ( $\delta f_{220}, \delta \tau_{220}$ ) impossible for those cases  
(see Appendix B for more details). On the other hand, the  
total mass threshold  $\geq 90 M_\odot$  was employed due to the fact  
that this analysis is computationally expensive and also  
because we expected these events to be the most promising  
for ringdown studies. However, since the SNR threshold  
alone should be sufficient for the analysis, for this paper, we  
run the test on all the events listed in Ref. [19] that have  
SNRs in the pre- and postmerger regions  $\geq 8$ , without  
imposing any mass threshold.  
524  
525  
526  
527  
528  
529  
530  
531  
532  
533  
534  
535  
536  
537  
538  
539  
540  
541  
542  
543  
544  
545  
546  
547  
548  
549  
550  
551  
552  
553  
554  
555  
556  
557  
558  
559  
560  
561

Given the above, we add the signals GW190630\_185205  
and GW190828\_063405 to the list of GW events considered  
in Ref. [19]. Furthermore, for the first time, we apply  
our method to measure the QNMs to GW events from O1  
and O2, notably GW150914 and GW170104. The other high-mass events from O1 and O2—GW170729,  
GW170809, GW170814, GW170818, and GW170823—  
do not have an  $\text{SNR} \geq 8$  in the merger-ringdown signal.  
562

<sup>4</sup>The pre- and postmerger regions of the signal are identified  
from the signal's power before and after the signal reaches the  
peak's amplitude, which is determined from the maximum of the  
likelihood function obtained with the parameter-estimation  
analysis. The SNR values are listed in Table IV of Ref. [19].  
563  
564  
565  
566  
567  
568  
569  
570  
571  
572  
573  
574  
575  
576  
577  
578  
579  
580  
581  
582  
583  
584  
585  
586  
587  
588  
589  
590  
591  
592  
593  
594  
595  
596  
597  
598  
599  
600  
601  
602  
603  
604  
605  
606  
607  
608  
609  
610  
611  
612  
613  
614  
615  
616  
617  
618  
619  
620  
621  
622  
623  
624  
625  
626  
627  
628  
629  
630  
631  
632  
633  
634  
635  
636  
637  
638  
639  
640  
641  
642  
643  
644  
645  
646  
647  
648  
649  
650  
651  
652  
653  
654  
655  
656  
657  
658  
659  
660  
661  
662  
663  
664  
665  
666  
667  
668  
669  
670  
671  
672  
673  
674  
675  
676  
677  
678  
679  
680  
681  
682  
683  
684  
685  
686  
687  
688  
689  
690  
691  
692  
693  
694  
695  
696  
697  
698  
699  
700  
701  
702  
703  
704  
705  
706  
707  
708  
709  
710  
711  
712  
713  
714  
715  
716  
717  
718  
719  
720  
721  
722  
723  
724  
725  
726  
727  
728  
729  
730  
731  
732  
733  
734  
735  
736  
737  
738  
739  
740  
741  
742  
743  
744  
745  
746  
747  
748  
749  
750  
751  
752  
753  
754  
755  
756  
757  
758  
759  
7510  
7511  
7512  
7513  
7514  
7515  
7516  
7517  
7518  
7519  
7520  
7521  
7522  
7523  
7524  
7525  
7526  
7527  
7528  
7529  
7530  
7531  
7532  
7533  
7534  
7535  
7536  
7537  
7538  
7539  
7540  
7541  
7542  
7543  
7544  
7545  
7546  
7547  
7548  
7549  
7550  
7551  
7552  
7553  
7554  
7555  
7556  
7557  
7558  
7559  
7560  
7561  
7562  
7563  
7564  
7565  
7566  
7567  
7568  
7569  
7570  
7571  
7572  
7573  
7574  
7575  
7576  
7577  
7578  
7579  
7580  
7581  
7582  
7583  
7584  
7585  
7586  
7587  
7588  
7589  
7590  
7591  
7592  
7593  
7594  
7595  
7596  
7597  
7598  
7599  
75100  
75101  
75102  
75103  
75104  
75105  
75106  
75107  
75108  
75109  
75110  
75111  
75112  
75113  
75114  
75115  
75116  
75117  
75118  
75119  
75120  
75121  
75122  
75123  
75124  
75125  
75126  
75127  
75128  
75129  
75130  
75131  
75132  
75133  
75134  
75135  
75136  
75137  
75138  
75139  
75140  
75141  
75142  
75143  
75144  
75145  
75146  
75147  
75148  
75149  
75150  
75151  
75152  
75153  
75154  
75155  
75156  
75157  
75158  
75159  
75160  
75161  
75162  
75163  
75164  
75165  
75166  
75167  
75168  
75169  
75170  
75171  
75172  
75173  
75174  
75175  
75176  
75177  
75178  
75179  
75180  
75181  
75182  
75183  
75184  
75185  
75186  
75187  
75188  
75189  
75190  
75191  
75192  
75193  
75194  
75195  
75196  
75197  
75198  
75199  
75200  
75201  
75202  
75203  
75204  
75205  
75206  
75207  
75208  
75209  
75210  
75211  
75212  
75213  
75214  
75215  
75216  
75217  
75218  
75219  
75220  
75221  
75222  
75223  
75224  
75225  
75226  
75227  
75228  
75229  
75230  
75231  
75232  
75233  
75234  
75235  
75236  
75237  
75238  
75239  
75240  
75241  
75242  
75243  
75244  
75245  
75246  
75247  
75248  
75249  
75250  
75251  
75252  
75253  
75254  
75255  
75256  
75257  
75258  
75259  
75260  
75261  
75262  
75263  
75264  
75265  
75266  
75267  
75268  
75269  
75270  
75271  
75272  
75273  
75274  
75275  
75276  
75277  
75278  
75279  
75280  
75281  
75282  
75283  
75284  
75285  
75286  
75287  
75288  
75289  
75290  
75291  
75292  
75293  
75294  
75295  
75296  
75297  
75298  
75299  
75300  
75301  
75302  
75303  
75304  
75305  
75306  
75307  
75308  
75309  
75310  
75311  
75312  
75313  
75314  
75315  
75316  
75317  
75318  
75319  
75320  
75321  
75322  
75323  
75324  
75325  
75326  
75327  
75328  
75329  
75330  
75331  
75332  
75333  
75334  
75335  
75336  
75337  
75338  
75339  
75340  
75341  
75342  
75343  
75344  
75345  
75346  
75347  
75348  
75349  
75350  
75351  
75352  
75353  
75354  
75355  
75356  
75357  
75358  
75359  
75360  
75361  
75362  
75363  
75364  
75365  
75366  
75367  
75368  
75369  
75370  
75371  
75372  
75373  
75374  
75375  
75376  
75377  
75378  
75379  
75380  
75381  
75382  
75383  
75384  
75385  
75386  
75387  
75388  
75389  
75390  
75391  
75392  
75393  
75394  
75395  
75396  
75397  
75398  
75399  
75400  
75401  
75402  
75403  
75404  
75405  
75406  
75407  
75408  
75409  
75410  
75411  
75412  
75413  
75414  
75415  
75416  
75417  
75418  
75419  
75420  
75421  
75422  
75423  
75424  
75425  
75426  
75427  
75428  
75429  
75430  
75431  
75432  
75433  
75434  
75435  
75436  
75437  
75438  
75439  
75440  
75441  
75442  
75443  
75444  
75445  
75446  
75447  
75448  
75449  
75450  
75451  
75452  
75453  
75454  
75455  
75456  
75457  
75458  
75459  
75460  
75461  
75462  
75463  
75464  
75465  
75466  
75467  
75468  
75469  
75470  
75471  
75472  
75473  
75474  
75475  
75476  
75477  
75478  
75479  
75480  
75481  
75482  
75483  
75484  
75485  
75486  
75487  
75488  
75489  
75490  
75491  
75492  
75493  
75494  
75495  
75496  
75497  
75498  
75499  
75500  
75501  
75502  
75503  
75504  
75505  
75506  
75507  
75508  
75509  
75510  
75511  
75512  
75513  
75514  
75515  
75516  
75517  
75518  
75519  
75520  
75521  
75522  
75523  
75524  
75525  
75526  
75527  
75528  
75529  
75530  
75531  
75532  
75533  
75534  
75535  
75536  
75537  
75538  
75539  
75540  
75541  
75542  
75543  
75544  
75545  
75546  
75547  
75548  
75549  
75550  
75551  
75552  
75553  
75554  
75555  
75556  
75557  
75558  
75559  
75560  
75561  
75562  
75563  
75564  
75565  
75566  
75567  
75568  
75569  
75570  
75571  
75572  
75573  
75574  
75575  
75576  
75577  
75578  
75579  
75580  
75581  
75582  
75583  
75584  
75585  
75586  
75587  
75588  
75589  
75590  
75591  
75592  
75593  
75594  
75595  
75596  
75597  
75598  
75599  
75600  
75601  
75602  
75603  
75604  
75605  
75606  
75607  
75608  
75609  
75610  
75611  
75612  
75613  
75614  
75615  
75616  
75617  
75618  
75619  
75620  
75621  
75622  
75623  
75624  
75625  
75626  
75627  
75628  
75629  
75630  
75631  
75632  
75633  
75634  
75635  
75636  
75637  
75638  
75639  
75640  
75641  
75642  
75643  
75644  
75645  
75646  
75647  
75648  
75649  
75650  
75651  
75652  
75653  
75654  
75655  
75656  
75657  
75658  
75659  
75660  
75661  
75662  
75663  
75664  
75665  
75666  
75667  
75668  
75669  
75670  
75671  
75672  
75673  
75674  
75675  
75676  
75677  
75678  
75679  
75680  
75681  
75682  
75683  
75684  
75685  
75686  
75687  
75688  
75689  
75690  
75691  
75692  
75693  
75694  
75695  
75696  
75697  
75698  
75699  
75700  
75701  
75702  
75703  
75704  
75705  
75706  
75707  
75708  
75709  
75710  
75711  
75712  
75713  
75714  
75715  
75716  
75717  
75718  
75719  
75720  
75721  
75722  
75723  
75724  
75725  
75726  
75727  
75728  
75729  
75730  
75731  
75732  
75733  
75734  
75735  
75736  
75737  
75738  
75739  
75740  
75741  
75742  
75743  
75744  
75745  
75746  
75747  
75748  
75749  
75750  
75751  
75752  
75753  
75754  
75755  
75756  
75757  
75758  
75759  
75760  
75761  
75762  
75763  
75764  
75765  
75766  
75767  
75768  
75769  
75770  
75771  
75772  
75773  
75774  
75775  
75776  
75777  
75778  
75779  
75780  
75781  
75782  
75783  
75784  
75785  
75786  
75787  
75788  
75789  
75790  
75791  
75792  
75793  
75794  
75795  
75796  
75797  
75798  
75799  
75800  
75801  
75802  
75803  
75804  
75805  
75806  
75807  
75808  
75809  
75810  
75811  
75812  
75813  
75814  
75815  
75816  
75817  
75818  
75819  
75820  
75821  
75822  
75823  
75824  
75825  
75826  
75827  
75828  
75829  
75830  
75831  
75832  
75833  
75834  
75835  
75836  
75837  
75838  
75839  
75840  
75841  
75842  
75843  
75844  
75845  
75846  
75847  
75848  
75849  
75850  
75851  
75852  
75853  
75854  
75855  
75856  
75857  
75858  
75859  
75860  
75861  
75862  
75863  
75864  
75865  
75866  
75867  
75868  
75869  
75870  
75871  
75872  
75873  
75874  
75875  
75876  
75877  
75878  
75879  
75880  
75881  
75882  
75883  
75884  
75885  
75886  
75887  
75888  
75889  
75890  
75891  
75892  
75893  
75894  
75895  
75896  
75897  
75898  
75899  
75900  
75901  
75902  
75903  
75904  
75905  
75906  
75907  
75908  
75909  
75910  
75911  
75912  
75913  
75914  
75915  
75916  
75917  
75918  
75919  
75920  
75921  
75922  
75923  
75924  
75925  
75926  
75927  
75928  
75929  
75930  
75931  
75932  
75933  
75934  
75935  
75936  
75937  
75938  
75939  
75940  
75941  
75942  
75943  
75944  
75945  
75946  
75947  
75948  
75949  
75950  
75951  
75952  
75953  
75954  
75955  
75956  
75957  
75958  
75959  
75960  
75961  
75962  
75963  
75964  
75965  
75966  
75967  
75968  
75969  
75970  
75971  
75972  
75973  
75974  
75975  
75976  
75977  
75978  
75979  
75980  
75981  
75982  
75983  
75984  
75985  
75986  
75987  
75988  
75989  
75990  
75991  
75992  
75993  
75994  
75995  
75996  
75997  
75998  
75999  
75100  
75101  
75102  
75103  
75104  
75105  
75106  
75107  
75108  
75109  
75110  
75111  
75112  
75113  
75114  
75115  
75116  
75117  
75118  
75119  
75120  
75121  
75122  
75123  
75124  
75125  
75126  
75127  
75128  
75129  
75130  
75131  
75132  
75133  
75134  
75135  
75136  
75137  
75138  
75139  
75140  
75141  
75142  
75143  
75144  
75145  
75146  
75147  
75148  
75149  
75150  
75151  
75152  
75153  
75154  
75155  
75156  
75157  
75158  
75159  
75160  
75161  
75162  
75163  
7516

TABLE II. The median and symmetric 90% credible intervals of the remnant properties. The first two columns represent the frequency and damping time of the (2,2) QNM measured using the pSEOBNR model. The next two columns are the mass and spin of the remnant object estimated from the complex QNM frequencies by inverting the fitting formula in Ref. [35]. The last two columns represent final mass and spin estimates predicted using NR fitting formulas from a SEOBNR parameter estimation.

Event	$f_{220}$ (Hz)	$\tau_{220}$ (ms)	$(1+z)M_f/M_\odot$	$\chi_f$	$(1+z)M_f^{\text{IMR}}/M_\odot$	$\chi_f^{\text{IMR}}$
GW150914	$257.6^{+17.0}_{-12.8}$	$4.49^{+1.09}_{-0.95}$	$71.0^{+8.7}_{-10.3}$	$0.77^{+0.09}_{-0.18}$	$67.3^{+2.7}_{-2.6}$	$0.67^{+0.03}_{-0.04}$
GW170104	$291.4^{+14.7}_{-30.1}$	$5.53^{+3.47}_{-2.40}$	$73.8^{+11.1}_{-19.8}$	$0.89^{+0.07}_{-0.36}$	$56.9^{+3.0}_{-3.0}$	$0.65^{+0.05}_{-0.07}$
GW190519_153544	$123.6^{+11.9}_{-13.0}$	$10.33^{+3.56}_{-3.07}$	$155.5^{+24.0}_{-29.9}$	$0.81^{+0.10}_{-0.28}$	$144.1^{+14.5}_{-16.2}$	$0.78^{+0.08}_{-0.14}$
GW190521_074359	$204.6^{+14.6}_{-11.7}$	$5.32^{+1.48}_{-1.21}$	$86.4^{+12.2}_{-14.3}$	$0.73^{+0.12}_{-0.26}$	$87.1^{+3.3}_{-3.8}$	$0.70^{+0.03}_{-0.05}$
GW190630_185205	$247.8^{+31.8}_{-52.8}$	$3.87^{+2.37}_{-1.80}$	$65.6^{+18.8}_{-41.5}$	$0.62^{+0.27}_{-0.62}$	$66.2^{+4.0}_{-3.2}$	$0.70^{+0.05}_{-0.08}$
GW190828_063405	$257.8^{+201.3}_{-27.8}$	$4.23^{+4.17}_{-1.92}$	$67.4^{+25.7}_{-30.0}$	$0.76^{+0.20}_{-0.73}$	$75.8^{+5.0}_{-5.0}$	$0.74^{+0.04}_{-0.06}$
GW190910_112807	$174.2^{+11.7}_{-7.5}$	$9.52^{+3.13}_{-2.68}$	$123.5^{+14.7}_{-18.1}$	$0.90^{+0.05}_{-0.11}$	$94.9^{+7.6}_{-8.6}$	$0.72^{+0.08}_{-0.04}$

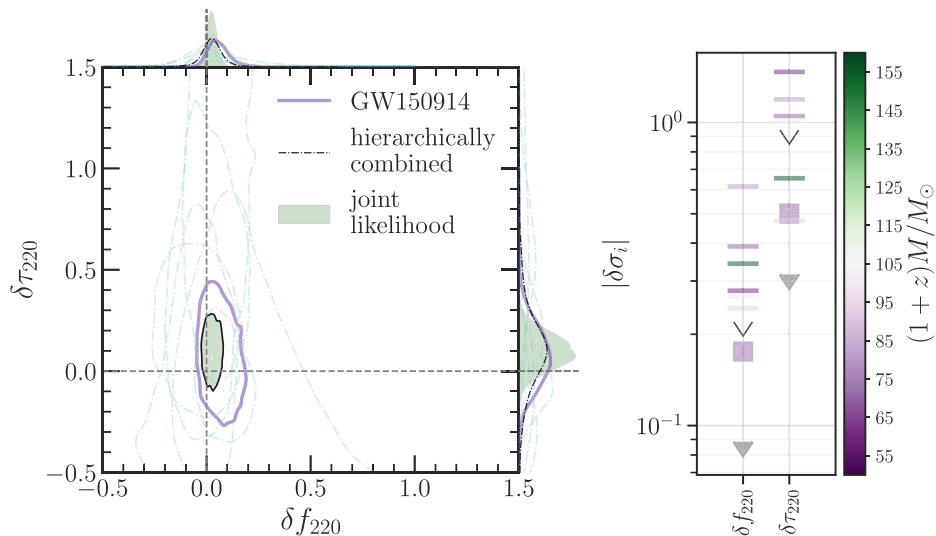
562 The list of the signals for which we run the analysis is given  
 563 in Table II.

564 For all the relevant signals, we show the posterior  
 565 distributions ( $\delta f_{220}$  and  $\delta \tau_{220}$ ) in the left panel in Fig. 6  
 566 and also provide the reconstructed QNM parameters ( $f_{220}$   
 567 and  $\tau_{220}$ ) in Table II. In the right panel in Fig. 6, we also  
 568 provide a summary of the 90% credible intervals on the 1D  
 569 marginalized posteriors. We highlight the dependence of  
 570 the constraints on the total mass of the system. In general,  
 571 the tightest bounds are set by the most massive systems, as  
 572 they tend to have a larger postmerger SNR. We find a  
 573 similar trend in the right panel in Fig. 6.

574 Among all the GW signals detected so far, GW150914  
 575 is unique in its loudness, leading to  
 576 the first and, to date, best attempt in measuring the QNM  
 577 frequencies [16,40,56,57]. Within 90% credibility, we  
 578 obtain from GW150914

$$\delta f_{220} = 0.05^{+0.11}_{-0.07}, \quad \delta \tau_{220} = 0.07^{+0.26}_{-0.23}. \quad (4.1)$$

580 Stronger constraints can be obtained by combining  
 582 information from all the events [19]. If we assume that  
 583 the fractional deviations ( $\delta f_{220}$  and  $\delta \tau_{220}$ ) take the same  
 584 values in multiple events, we can assume the posterior of



F6:1 FIG. 6. Left panel: the 90% credible levels of the posterior probability distribution of the fractional deviations in the frequency and damping time of the (2,2) QNM ( $\delta f_{220}$  and  $\delta \tau_{220}$ ) and their corresponding one-dimensional marginalized posterior distributions, for F6:2 events from O1, O2, and O3a passing a SNR threshold of 8 in both the pre- and postmerger signal. The solid purple curve marks the best F6:3 single-event constraint, GW150914, whereas the constraints from the other events are indicated by the dash-dotted curves. The joint F6:4 constraints on  $(\delta f_{220}, \delta \tau_{220})$  obtained multiplying the likelihoods from individual events are given by the filled gray contours, while the F6:5 hierarchical method of combination yields the black dot-dashed curves (shown only in the 1D posteriors plots). Right panel: 90% F6:6 credible interval on the one-dimensional marginalized posteriors on  $\delta \sigma_i = (\delta f_{220}, \delta \tau_{220})$ , colored by the median redshifted total mass F6:7  $(1+z)M_f/M_\odot$ , inferred assuming GR. Filled gray (unfilled black) triangles mark the constraints obtained when all the events are combined F6:8 by multiplying likelihoods (hierarchically). The purple square marker indicates constraints from the single most-prominent event, F6:9 GW150914. F6:10

585 one event to be the prior for the next and obtain a joint  
 586 posterior probability distribution. For  $N$  observations,  
 587 where  $P(\delta f_{220}, \delta \tau_{220}|d_j)$  is the posterior for the  $j$ th obser-  
 588 vation corresponding to the dataset  $d_j$ ,  $j = 1, \dots, N$ , the  
 589 joint posterior is given by

$$\begin{aligned} P(\delta f_{220}, \delta \tau_{220}|\{d_j\}) \\ = P(\delta f_{220}, \delta \tau_{220}) \prod_{j=1}^N \frac{P(\delta f_{220}, \delta \tau_{220}|d_j)}{P(\delta f_{220}, \delta \tau_{220})}, \end{aligned} \quad (4.2)$$

590 where  $P(\delta f_{220}, \delta \tau_{220})$  is the prior on  $(\delta f_{220}, \delta \tau_{220})$ .  
 592 However, since here we assume the prior on  $(\delta f_{220}, \delta \tau_{220})$   
 593 to be flat (or uniform), the joint posterior is equal to the joint  
 594 likelihood. We show these joint likelihoods on  $(\delta f_{220}, \delta \tau_{220})$ ,  
 595 as well as the corresponding 1D marginalized distributions,  
 596 as filled gray curves in Fig. 6. From the joint likelihood, we  
 597 obtain within 90% credibility

$$\delta f_{220} = 0.02^{+0.04}_{-0.04}, \quad \delta \tau_{220} = 0.10^{+0.14}_{-0.14}. \quad (4.3)$$

600 However, in most non-GR theories, the deviation param-  
 601 eters ( $\delta f_{220}$  and  $\delta \tau_{220}$ ) depend, in general, on the source's  
 602 parameters, so if GR were to be wrong, one should expect  
 603 their value to vary across the GW signals observed by  
 604 LIGO and Virgo. As described in Ref. [19], we can relax  
 605 the assumption of a constant deviation across all events by  
 606 using the hierarchical inference technique originally pro-  
 607 posed in Refs. [93,94]. The general idea behind this  
 608 technique is to assume that the non-GR parameters  
 609 ( $\delta f_{220}$  and  $\delta \tau_{220}$ ) are drawn from a common underlying  
 610 distribution, whose properties can be inferred from the  
 611 population of events. Following Refs. [19,93,94], we model  
 612 the population distribution with a Gaussian  $\mathcal{N}(\mu, \sigma)$  of  
 613 unknown mean  $\mu$  and standard deviation  $\sigma$ . Under those  
 614 assumptions, the goal is then to directly measure a posterior  
 615 distribution  $P(\mu, \sigma|\{d_j\})$  for  $\mu$  and  $\sigma$  from a joint analysis  
 616 of all the GW events. If GR is correct, then this posterior  
 617 should be consistent with  $\mu = 0$  and  $\sigma = 0$ . From the Bayes  
 618 theorem, it follows that [94]

$$P(\mu, \sigma|\{d_j\}) \propto P(\mu, \sigma) \prod_{j=1}^N P(d_j|\mu, \sigma), \quad (4.4)$$

620 where  $P(\mu, \sigma)$  is the prior (also known as hyperprior) on  
 621  $(\mu, \sigma)$  and  $P(d_j|\mu, \sigma)$  can be written in terms of the  
 622 individual likelihoods of a given non-GR parameter  $\xi_{\text{nGR}}$   
 623 using [94]

$$P(d_j|\mu, \sigma) = \int P(d_j|\xi_{\text{nGR}})P(\xi_{\text{nGR}}|\mu, \sigma)d\xi_{\text{nGR}}. \quad (4.5)$$

624 Here,  $P(\xi_{\text{nGR}}|\mu, \sigma) = \mathcal{N}(\mu, \sigma)$  by construction and  
 626  $P(d_j|\xi_{\text{nGR}})$  is the likelihood for the parameter  $\xi_{\text{nGR}}$  for a

given event  $d_j$  that is computed from the standard parameter-estimation analysis. After obtaining  $P(\mu, \sigma|\{d_j\})$ , we can then infer a population distribution for a given non-GR parameter  $\xi_{\text{nGR}}$  using [94]

$$P(\xi_{\text{nGR}}|\{d_j\}) = \int P(\xi_{\text{nGR}}|\mu, \sigma)P(\mu, \sigma|\{d_j\})d\mu d\sigma. \quad (4.6)$$

Notice that, if we fix  $\sigma = 0$ , this approach is equivalent to assuming that all events share the same non-GR parameter  $\xi_{\text{nGR}} = \mu$  and Eq. (4.6) reduces to the joint likelihood [93]. In practice, we use the STAN-based code [95] developed and used in Refs. [19,94] to obtain  $P(\mu, \sigma|\{d_j\})$  and compute  $P(\xi_{\text{nGR}}|\{d_j\})$ . We note that the current implementation of this analysis, as originally defined in Ref. [94], is defined only for 1D posteriors; therefore, below, we show only 1D posteriors for the hierarchical analysis.

The posteriors for  $\delta f_{220}$  and  $\delta \tau_{220}$  obtained with this technique are shown in Fig. 6 (dash-dotted curves) with the corresponding median and 90% credible interval given by

$$\delta f_{220} = 0.03^{+0.10}_{-0.09}, \quad \delta \tau_{220} = 0.10^{+0.44}_{-0.39}. \quad (4.7)$$

Compared to Ref. [19], these constraints are almost a factor of  $\sim 4$  more stringent for  $\delta f_{220}$  and a factor of  $\sim 2$  for  $\delta \tau_{220}$ . Similar improvements hold for the hyperparameters:  $\delta f_{220}(\mu = 0.03^{+0.06}_{-0.05}, \sigma < 0.09)$  and  $\delta \tau_{220}(\mu = 0.11^{+0.21}_{-0.19}, \sigma < 0.39)$ .

## V. DISCUSSION

We have built a parameterized IMR waveform model, pSEOBNR, that can measure the QNM complex frequencies of the remnant object formed through the merger of BHs with aligned or antialigned spins, thus extending previous work, which was limited to nonspinning BHs [56]. The pSEOBNR model was recently used to infer the QNMs of some of the BBH's remnants detected by LIGO and Virgo during O3a [19].

After testing our method to infer the QNM frequencies with GR and non-GR synthetic-signal injections in Gaussian noise, we have applied it to LIGO and Virgo real data. We have analyzed GW events in O1, O2, and O3a (a total of four new events) that were not examined in Ref. [19] with the pSEOBNR model (see Table II). After combining our new results with the other GW events in O3a investigated with our method [19], we have obtained more stringent bounds on the dominant (or least-damped) QNM ( $\ell = 2, m = 2$ ).

More specifically, as expected, the single GW event providing the best constraint on the least-damped QNM to date continues to be GW150914 ( $\delta f_{220} = 0.05^{+0.11}_{-0.07}$  and  $\delta \tau_{220} = 0.07^{+0.26}_{-0.23}$ ), although the bounds on  $\delta \tau_{220}$  from GW150914 are comparable to GW190521\_074359, the second-most precisely measured

event in our list. In addition, in the most agnostic and conservative scenario where we combine the information from different events using a hierarchical approach [93,94], we obtain at 90% credibility ( $\delta f_{220} = 0.03^{+0.10}_{-0.09}$  and  $\delta \tau_{220} = 0.10^{+0.44}_{-0.39}$ ). Thus, our results constrain the frequency (decay time) of the least-damped QNM to be within  $\sim 10\%$  ( $\sim 40\%$ ) of the GR prediction—an improvement of a factor of  $\sim 4$  ( $\sim 2$ ) over the results obtained with the pSEOBNR model in Ref. [19].

Furthermore, when assuming that the deviations from GR do not vary appreciably over the GW events that we have analyzed and combining the likelihood functions, we have obtained the most stringent bounds on the dominant QNM ( $\delta f_{220} = 0.02^{+0.04}_{-0.04}$  and  $\delta \tau_{220} = 0.10^{+0.14}_{-0.14}$ ). Those constraints are compatible with but slightly better (especially for the decay time) than the ones recently reported in Ref. [96] (see the first row in Table II therein), where QNM frequencies were inferred using only the postmerger part of the signal. We note that Ref. [96] used a larger set of GW events from O1, O2, and O3a than we did, although we expect that the extra GW events will not contribute significantly to the combined bound, since they have lower SNRs.

These constraints could, in principle, be used to constrain specific non-GR theories and exotic compact objects [97–99]. However, QNM computations in non-GR theories have been done only in a handful of cases, mostly focusing on nonrotating or slowly rotating BH solutions [100–117] or relying on the eikonal or geometric optics approximation to obtain estimates of the QNMs for spinning BHs [103,118,119]. The only exceptions to this rule, that we are aware of, are computations of the QNM of Kerr-Newman BHs in Einstein-Maxwell theory [120–123] or estimates of the BBH in non-GR theories obtained through a limited number of NR simulations [124,125]. Given these limitations, our ability of going beyond a null test of GR and using our results to impose precise constraints on non-GR theories with QNM measurements is currently quite limited.

Despite these theoretical limitations, there has been some recent effort to develop parametrizations that could help map measurements of the parameters ( $\delta f_{\ell m 0}$  and  $\delta \tau_{\ell m 0}$ ) onto constraints to specific non-GR theories. This includes, for example, the parametrization proposed in Ref. [43], recently applied to LIGO-Virgo GW events in Ref. [96], where deviations from the GR QNMs explicitly depend on a perturbative expansion in the BH spin and possible extra non-GR parameters, or the proposal of Refs. [126,127], where deviations from the GR QNMs are mapped onto generic small modifications of the perturbation equations describing the QNMs. Other examples also include proposals to map deviations from the GR QNMs to coefficients in generic effective-field-theory actions [106,107,115] or to directly relate measurements of the QNM complex frequencies to a parametrized non-GR BH metric [118,128,129], which could be then used jointly with measurements from the Event Horizon Telescope to obtain stronger constraints on

deviations from GR [129–132]. We should note, however, that all these parametrizations are either limited to non-spinning BHs or make use of a series expansion in the BH spin which might limit their accuracy for highly spinning BHs, unless the sensitivity of GW detectors will not allow us to access the higher coefficients in the spin series.

In the future, it would be important to test whether the pSEOBNR model could be used to detect deviations in waveforms obtained through NR simulations of specific non-GR theories. Such results are still in their infancy and have so far been done only for a handful of theories, focusing mostly on proof-of-concept simulations [124,125,133–140]. Nonetheless, given the recent efforts put forward in order to simulate BBHs in non-GR theories, we hope that accurate non-GR IMR waveforms will become available in the near future.

Finally, an obvious generalization of this work would be to extend the parameterized pSEOBNR model to generic precessing BBHs, which can, in principle, be easily done using the recently developed multipolar EOB model reported in Ref. [141]. Lastly, it will be relevant to include GR deviations in the pSEOBNR model also during the late inspiral and plunge stages of the BBH coalescence. On the other hand, GR deviations (notably, deviations from PN theory) for the long inspiral stage are currently available in the pSEOBNR model and have been used to set bounds on the PN parameters in the GW phasing using LIGO and Virgo observations [17–19].

## ACKNOWLEDGMENTS

The authors thank Max Isi, for generously allowing us to use the code developed in Ref. [94] for the hierarchical inference analysis, and Gregorio Carullo, for carefully reading the manuscript and providing useful comments. The authors are grateful for computational resources provided by the LIGO Laboratory and supported by the National Science Foundation Grants No. PHY-0757058 and No. PHY-0823459, as well as computational resources at the Albert Einstein Institute, specifically the Hypatia cluster. R. B. acknowledges financial support from the European Union’s Horizon 2020 research and innovation program under the Marie Skłodowska-Curie Grant Agreement No. 792862, from the European Union’s H2020 ERC, Starting Grant Agreement No. DarkGRA-757480, and from the MIUR PRIN and FARE programs (GW-NEXT, CUP: B84I20000100001). We also acknowledge support from the Amaldi Research Center funded by the MIUR program “Dipartimento di Eccellenza” (CUP: B81I18001170001).

## APPENDIX A: STUDY OF SYSTEMATICS IN RINGDOWN MEASUREMENTS IN REAL, NON-GAUSSIAN NOISE

Inferences of all parameters in this paper have been done under the assumption that the noise in the detectors is

stationary and Gaussian. In other words, detector noise follows a normal distribution with zero mean and a PSD,  $S_n(f)$ , that is not a function of time, at least during the duration of the GW signal. This allows us to write the Bayesian likelihood function in the form given in Eqs. (2.10) and (2.11) and perform all the parameter estimation that follows in the results sections. However, LIGO-Virgo noise can often have features that deviate from stationarity and Gaussianity. If such features are not taken into account appropriately, final estimates of parameters can get biased. Here, we demonstrate one such case by injecting in real noise a GW190521-like signal and showing how parameter estimates can be biased when our description of detector noise is not complete.

We choose a spinning, precessing NR-surrogate model NRSur<sup>5</sup> (valid up to mass ratio 4) to simulate the actual GW190521 signal observed by the LIGO and Virgo detectors [54] (see Table I in Ref. [54]). The choice of the NRSur model is motivated by the fact that it is the most accurate model in the parameter range described by GW190521, because it is built by directly interpolating NR waveforms. In Fig. 7, we indicate with a black cross what the injected NRSur signal predicts for the QNM ( $\ell = 2$  and  $m = 2$ ) frequency and damping time. For comparison, we also show with a black solid curve the results obtained when recovering the actual signal GW190521 with the pSEOBNR model. As seen in the plot, while the measurement of the frequency is consistent with the prediction, we overestimate the damping time.

To understand such an offset in the decay time, we proceed as follows. The actual GW190521 event was observed at a GPS time, 1242442967.61 s (roughly 03:02:49 UTC, May 21, 2019). We select a time period of about 2.5 h around this GPS time, create synthetic signals with the NRSur model, and inject them in different stretches of the real detector noise around the time of the actual GW event. The PSDs of GW detectors are expected to vary over longer durations of time, and hence the 2.5 h stretch of noise we consider can be assumed to have noise properties similar to the time of the actual event. Then, we perform Bayesian analysis against those injections using the pSEOBNR model. The results are indicated by green curves in Fig. 7. As can be seen from the figure, for three of the five noise realizations, corresponding to  $t_0 - 1$  h,  $t_0 + 0.5$  h, and  $t_0 + 1$  h, respectively, we recover a damping time similar to the one obtained when using the pSEOBNR model against the actual event GW190521 (black curve), where  $t_0$  is the GPS time of the actual event. For the other two noise realizations, the pSEOBNR model estimates consistently the damping time but has an offset frequency, while the fifth noise realization is consistent with both predictions. This study suggests that a bias in the measurements of the damping time for the actual

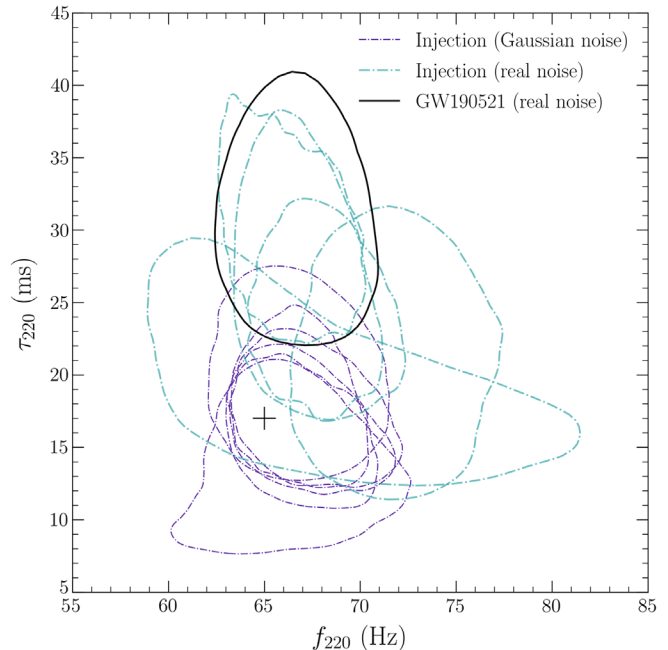


FIG. 7. 90% credible level on the posterior probability distribution of the frequency and damping time of (2,2) mode ( $f_{220}^{\text{GR}}$  and  $\tau_{220}^{\text{GR}}$ ) using synthetic NRSur signals with parameters similar to the GW event GW190521, in Gaussian noise (gray dot-dashed lines) and real interferometric noise (green dot-dashed lines). The GR prediction for the frequency and damping time is indicated by the black cross. While the Gaussian noise simulations are consistent with the prediction, at least three of the five real noise simulations are not. The black curve corresponds to the measurements of the real event GW190521 reported in Ref. [19]. All signals are recovered using the pSEOBNR model.

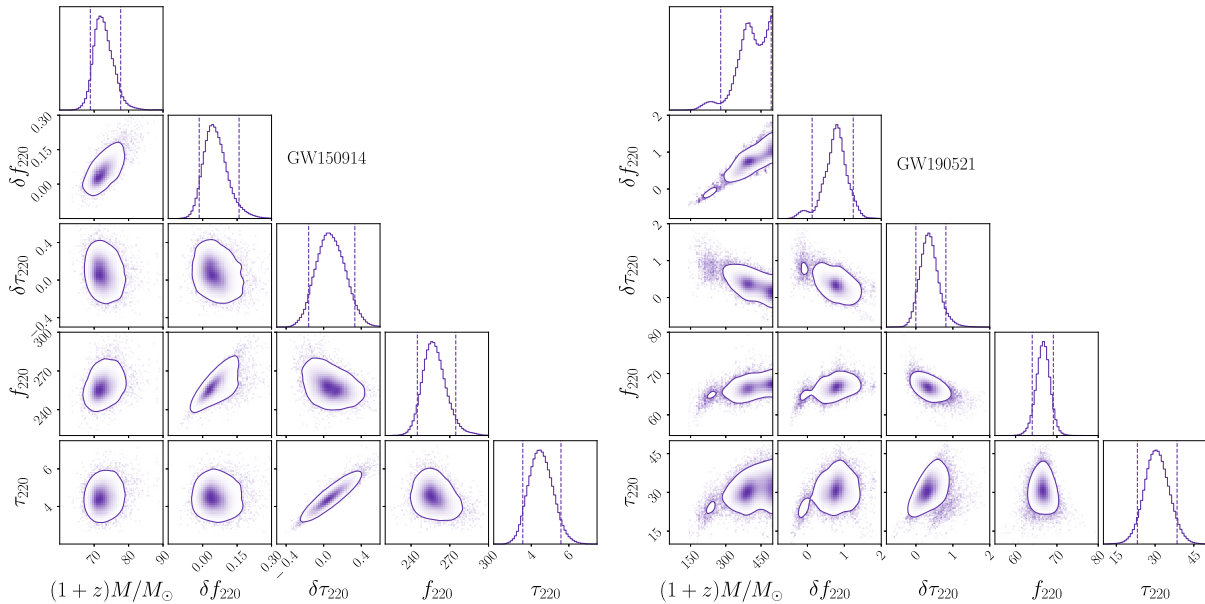
F7:1  
F7:2  
F7:3  
F7:4  
F7:5  
F7:6  
F7:7  
F7:8  
F7:9  
F7:10  
F7:11

event GW190521 can be explained as due to an incomplete description of the noise at the time of the event.

The reader might question the judiciousness of using an aligned-spin waveform model, like pSEOBNR, to measure a signal like GW190521 which appears to be precessing, especially because an incomplete understanding of the underlying signal can also lead to biases in measured quantities, as we have already demonstrated in Sec. III B. In order to explore possible effects of missing information about in-plane spins in the pSEOBNR model, we repeat the above study of injecting synthetic signals using NRSur and recovering using the pSEOBNR model, but this time, instead of using real detector noise, we use Gaussian noise (i.e., realizations of noise sampled from a predicted detector PSD). Since the properties of the noise are completely understood in this case, any residual measurement biases can be completely attributed to differences in the waveform model. The 2D posterior distributions of the frequency and damping time measured using these Gaussian-noise signals are shown by the gray curves in Fig. 7. We find the measurements to be completely consistent with the predictions of the frequency and damping time, thus concluding that a lack of in-plane spins in the pSEOBNR model

835  
836  
837  
838  
839  
840  
841  
842  
843  
844  
845  
846  
847  
848  
849  
850  
851  
852  
853  
854  
855  
856

<sup>5</sup>This waveform model is called NRSur7dq4 in LAL.



F8:1 FIG. 8. Corner plots showing the correlations between the detector-frame total F8:2 ( $1 + z$ ) $M$ , the non-GR deviations ( $\delta f_{220}$  and  $\delta \tau_{220}$ ), and F8:3 the reconstructed frequency and damping time ( $f_{220}$  and  $\tau_{220}$ ). The left panel shows results for F8:4 GW150914, for which  $\text{SNR} > 8$  in both the pre- and postmerger phase of the signal, and the correlations are absent. The right panel shows the results for GW190521, which has  $\text{SNR} > 8$  in the postmerger phase but not in the premerger phase, and the correlations are present.

does not affect our measurements of the QNM properties. The fact that the measurement of ringdown quantities is robust against an incomplete description of the inspiral signal is a crucial property of our method.

## APPENDIX B: CORRELATION OF THE BINARY'S TOTAL MASS WITH THE NON-GR PARAMETERS

As mentioned in the main text, for low-SNR events with negligible higher modes and for which only the postmerger is detectable, there is a strong degeneracy between the binary's total mass and the non-GR deviations ( $\delta f_{220}$  and  $\delta \tau_{220}$ ). For those cases, only the reconstructed frequency and damping time ( $f_{220}$  and  $\tau_{220}$ ) can be independently measured from the data. To justify this statement, in Fig. 8 we show corner plots that illustrate the correlations between the non-GR parameters ( $\delta f_{220}$  and  $\delta \tau_{220}$ ), the detector-frame total mass  $M(1 + z)$ , and the reconstructed frequency and damping time ( $f_{220}$  and  $\tau_{220}$ ) for GW150914 (left panel),

corresponding to an event for which both the pre- and postmerger phases are measurable, and for GW190521 (right panel), an event in which the postmerger has  $\text{SNR} > 8$ , but the premerger has an SNR below 8. For GW190521, due to the strong degeneracy between  $\delta f_{220}$  and  $M(1 + z)$ , the 1D posterior for  $M(1 + z)$  is pushed toward the upper boundary of its prior, despite the very wide prior employed in the analysis. This, in turn, renders the measurement of  $\delta f_{220}$  (and, to a lesser degree, of  $\delta \tau_{220}$ ) highly dependent on the upper boundary of the total mass prior. On the other hand, this issue does not significantly affect the posteriors for the reconstructed quantities ( $f_{220}$  and  $\tau_{220}$ ) which are well measured and nearly independent on the upper prior boundary for  $M(1 + z)$ . This is to be contrasted with the results for GW150914. In this case, the extra information coming from the premerger phase allows one to break the degeneracy between the non-GR parameters and the total mass, and, therefore, both ( $\delta f_{220}, \delta \tau_{220}$ ) and  $M(1 + z)$  can be measured at the same time.

- |     |  |   |     |
|-----|--|---|-----|
| 896 | [1] LIGO Scientific Collaboration, <a href="https://www.ligo.org/">https://www.ligo.org/</a> .                                     | 8 | 902 |
| 897 | [2] Virgo Collaboration, <a href="https://www.virgo-gw.eu/">https://www.virgo-gw.eu/</a> .   |   | 903 |
| 898 | [3] R. Abbott <i>et al.</i> (LIGO Scientific, Virgo Collaborations), arXiv:2010.14527 [Phys. Rev. X (to be published)].            |   | 904 |
| 899 | [4] B. P. Abbott <i>et al.</i> (LIGO Scientific, Virgo Collaborations), Phys. Rev. X <b>9</b> , 031040 (2019).                     |   | 905 |
| 900 | [5] J. Aasi <i>et al.</i> (LIGO Scientific Collaboration), Classical Quantum Gravity <b>32</b> , 115012 (2015).                    |   | 906 |
| 901 | [6] F. Acernese <i>et al.</i> (VIRGO Collaboration), Classical Quantum Gravity <b>32</b> , 024001 (2015).                          |   | 907 |
|     | [7] A. H. Nitz, C. Capano, A. B. Nielsen, S. Reyes, R. White, D. A. Brown, and B. Krishnan, Astrophys. J. <b>872</b> , 195 (2019). |   |     |

- 908 [8] A. H. Nitz, T. Dent, G. S. Davies, S. Kumar, C. D. Capano,  
909 I. Harry, S. Mozzon, L. Nuttall, A. Lundgren, and M.  
910 Tápai, *Astrophys. J.* **891**, 123 (2019).
- 911 [9] T. Venumadhav, B. Zackay, J. Roulet, L. Dai, and M.  
912 Zaldarriaga, *Phys. Rev. D* **101**, 083030 (2020).
- 913 [10] B. Zackay, L. Dai, T. Venumadhav, J. Roulet, and M.  
914 Zaldarriaga, arXiv:1910.09528.
- 915 [11] B. P. Abbott *et al.* (LIGO Scientific, Virgo Collaborations),  
916 *Phys. Rev. Lett.* **116**, 061102 (2016).
- 917 [12] B. P. Abbott *et al.* (LIGO Scientific, Virgo Collaborations),  
918 *Astrophys. J. Lett.* **818**, L22 (2016).
- 919 [13] B. P. Abbott *et al.* (LIGO Scientific, Virgo, Fermi GBM,  
920 INTEGRAL, IceCube, AstroSat Cadmium Zinc Telluride  
921 Imager Team, IPN, Insight-Hxmt, ANTARES, Swift,  
922 AGILE Team, 1M2H Team, Dark Energy Camera GW-  
923 EM, DES, DLT40, GRAWITA, Fermi-LAT, ATCA, AS-  
924 KAP, Las Cumbres Observatory Group, OzGrav, DWF  
925 (Deeper Wider Faster Program), AST3, CAASTRO,  
926 VINROUGE, MASTER, J-GEM, GROWTH, JAGWAR,  
927 CaltechNRAO, TTU-NRAO, NuSTAR, Pan-STARRS,  
928 MAXI Team, TZAC Consortium, KU, Nordic Optical  
929 Telescope, ePESSTO, GROND, Texas Tech University,  
930 SALT Group, TOROS, BOOTES, MWA, CALET, IKI-  
931 GW Follow-up, H.E.S.S., LOFAR, LWA, HAWC, Pierre  
932 Auger, ALMA, Euro VLBI Team, Pi of Sky, Chandra  
933 Team at McGill University, DFN, ATLAS Telescopes,  
934 High Time Resolution Universe Survey, RIMAS, RATIR,  
935 SKA South Africa/MeerKAT Collaborations), *Astrophys.  
936 J. Lett.* **848**, L12 (2017).
- 937 [14] B. P. Abbott *et al.* (LIGO Scientific, Virgo, Fermi-GBM,  
938 INTEGRAL Collaborations), *Astrophys. J. Lett.* **848**, L13  
939 (2017).
- 940 [9] [15] B. P. Abbott *et al.* (LIGO Scientific, Virgo, 1M2H, Dark  
941 Energy Camera GW-E, DES, DLT40, Las Cumbres  
942 Observatory, VINROUGE, MASTER Collaborations),  
943 *Nature (London)* **551**, 425 (2017).
- 944 [16] B. P. Abbott *et al.* (LIGO Scientific, Virgo Collaborations),  
945 *Phys. Rev. Lett.* **116**, 221101 (2016); **121**, 129902(E)  
946 (2018).
- 947 [17] B. P. Abbott *et al.* (LIGO Scientific, Virgo Collaborations),  
948 *Phys. Rev. Lett.* **123**, 011102 (2019).
- 949 [18] B. P. Abbott *et al.* (LIGO Scientific, Virgo Collaborations),  
950 *Phys. Rev. D* **100**, 104036 (2019).
- 951 [19] R. Abbott *et al.* (LIGO Scientific, Virgo Collaborations),  
952 arXiv:2010.14529.
- 953 [20] L. Blanchet, *Living Rev. Relativity* **17**, 2 (2014).
- 954 [21] F. Pretorius, *Phys. Rev. Lett.* **95**, 121101 (2005).
- 955 [22] M. Campanelli, C. O. Lousto, P. Marronetti, and Y.  
956 Zlochower, *Phys. Rev. Lett.* **96**, 111101 (2006).
- 957 [23] J. G. Baker, J. Centrella, D.-I. Choi, M. Koppitz, and J. van  
958 Meter, *Phys. Rev. Lett.* **96**, 111102 (2006).
- 959 [24] C. V. Vishveshwara, *Nature (London)* **227**, 936 (1970).
- 960 [25] C. V. Vishveshwara, *Phys. Rev. D* **1**, 2870 (1970).
- 961 [26] W. H. Press, *Astrophys. J. Lett.* **170**, L105 (1971).
- 962 [27] S. Chandrasekhar and S. L. Detweiler, *Proc. R. Soc. A* **344**,  
963 441 (1975).
- 964 [28] S. L. Detweiler, *Astrophys. J.* **239**, 292 (1980).
- 965 [29] W. Israel, *Phys. Rev.* **164**, 1776 (1967).
- 966 [30] S. W. Hawking, *Commun. Math. Phys.* **25**, 152 (1972).
- 967 [31] B. Carter, *Phys. Rev. Lett.* **26**, 331 (1971).
- [32] D. C. Robinson, *Phys. Rev. Lett.* **34**, 905 (1975). 968
- [33] P. O. Mazur, *J. Phys. A* **15**, 3173 (1982). 969
- [34] O. Dreyer, B. J. Kelly, B. Krishnan, L. S. Finn, D. 970 Garrison, and R. Lopez-Aleman, *Classical Quantum Gravity* **21**, 787 (2004). 971
- [35] E. Berti, V. Cardoso, and C. M. Will, *Phys. Rev. D* **73**, 973 064030 (2006). 974
- [36] S. Gossan, J. Veitch, and B. S. Sathyaprakash, *Phys. Rev. D* **85**, 124056 (2012). 975
- [37] J. Meidam, M. Agathos, C. Van Den Broeck, J. Veitch, 976 and B. S. Sathyaprakash, *Phys. Rev. D* **90**, 064009 977 (2014). 978
- [38] G. Carullo *et al.*, *Phys. Rev. D* **98**, 104020 (2018). 979
- [39] G. Carullo, G. Riemschneider, K. W. Tsang, A. Nagar, 980 and W. Del Pozzo, *Classical Quantum Gravity* **36**, 105009 981 (2019). 982
- [40] M. Isi, M. Giesler, W. M. Farr, M. A. Scheel, and S. A. 983 Teukolsky, *Phys. Rev. Lett.* **123**, 111102 (2019). 984
- [41] S. Bhagwat, M. Cabero, C. D. Capano, B. Krishnan, and 985 D. A. Brown, *Phys. Rev. D* **102**, 024023 (2020). 986
- [42] M. Cabero, J. Westerweck, C. D. Capano, S. Kumar, A. B. 987 Nielsen, and B. Krishnan, *Phys. Rev. D* **101**, 064044 988 (2020). 989
- [43] A. Maselli, P. Pani, L. Gualtieri, and E. Berti, *Phys. Rev. D* 990 **101**, 024043 (2020). 991
- [44] K. G. Arun, B. R. Iyer, M. S. S. Qusailah, and B. S. 992 Sathyaprakash, *Phys. Rev. D* **74**, 024006 (2006). 993
- [45] K. G. Arun, B. R. Iyer, M. S. S. Qusailah, and B. S. 994 Sathyaprakash, *Classical Quantum Gravity* **23**, L37 995 (2006). 996
- [46] M. Agathos, W. Del Pozzo, T. G. F. Li, C. Van Den Broeck, 997 J. Veitch, and S. Vitale, *Phys. Rev. D* **89**, 082001 (2014). 998
- [47] B. P. Abbott *et al.* (LIGO Scientific, VIRGO Collaborations), *Phys. Rev. Lett.* **118**, 221101 (2017); **121**, 129901 999 (E) (2018). 1000
- [48] A. Samajdar and K. G. Arun, *Phys. Rev. D* **96**, 104027 1001 (2017). 1002
- [49] B. P. Abbott *et al.* (LIGO Scientific, Virgo Collaborations), 1003 *Phys. Rev. Lett.* **119**, 141101 (2017). 1004
- [50] M. Isi and A. J. Weinstein, arXiv:1710.03794. 1005
- [51] A. Ghosh *et al.*, *Phys. Rev. D* **94**, 021101(R) (2016). 1006
- [52] A. Ghosh, N. K. Johnson-McDaniel, A. Ghosh, C. K. 1007 Mishra, P. Ajith, W. Del Pozzo, C. P. Berry, A. B. Nielsen, 1008 and L. London, *Classical Quantum Gravity* **35**, 014002 1009 (2018). 1010
- [53] S. Ghonge, K. Chatzioannou, J. A. Clark, T. Littenberg, 1011 M. Millhouse, L. Cadonati, and N. Cornish, *Phys. Rev. D* 1012 **102**, 064056 (2020). 1013
- [54] R. Abbott *et al.* (LIGO Scientific, Virgo Collaborations), 1014 *Phys. Rev. Lett.* **125**, 101102 (2020). 1015
- [55] R. Abbott *et al.* (LIGO Scientific, Virgo Collaborations), 1016 *Astrophys. J. Lett.* **900**, L13 (2020). 1017
- [56] R. Brito, A. Buonanno, and V. Raymond, *Phys. Rev. D* **98**, 1018 084038 (2018). 1019
- [57] G. Carullo, W. Del Pozzo, and J. Veitch, *Phys. Rev. D* **99**, 1020 123029 (2019); **100**, 089903(E) (2019). 1021
- [58] J. C. Bustillo, P. D. Lasky, and E. Thrane, *Phys. Rev. D* 1022 **103**, 024041 (2021). 1023
- [59] M. Giesler, M. Isi, M. A. Scheel, and S. Teukolsky, *Phys. 1024 Rev. X* **9**, 041060 (2019). 1025
- [60] M. Giesler, M. Isi, M. A. Scheel, and S. Teukolsky, *Phys. 1026 Rev. X* **9**, 041060 (2019). 1027

- 1028 [60] M. Cabero, C. D. Capano, O. Fischer-Birnholtz, B.  
1029 Krishnan, A. B. Nielsen, A. H. Nitz, and C. M. Biwer,  
1030 *Phys. Rev. D* **97**, 124069 (2018).
- 1031 [61] M. Isi, W. M. Farr, M. Giesler, M. A. Scheel, and S. A.  
1032 Teukolsky, arXiv:2012.04486 [Phys. Rev. Lett. (to be  
1033 published)].
- 1034 [62] G. Carullo, D. Laghi, J. Veitch, and W. Del Pozzo, *Phys.*  
1035 *Rev. Lett.* **126**, 161102 (2021).
- 1036 [63] V. F. Foit and M. Kleban, *Classical Quantum Gravity* **36**,  
1037 035006 (2019).
- 1038 [64] D. Laghi, G. Carullo, J. Veitch, and W. Del Pozzo,  
1039 *Classical Quantum Gravity* **38**, 095005 (2021).
- 1040 [65] A. B. Nielsen, C. D. Capano, O. Birnholtz, and J. Westerweck,  
1041 *Phys. Rev. D* **99**, 104012 (2019).
- 1042 [66] K. W. Tsang, A. Ghosh, A. Samajdar, K. Chatzioannou, S.  
1043 Mastrogiovanni, M. Agathos, and C. Van Den Broeck,  
1044 *Phys. Rev. D* **101**, 064012 (2020).
- 1045 [67] R. Lo, T. Li, and A. Weinstein, *Phys. Rev. D* **99**, 084052  
1046 (2019).
- 1047 [68] J. Abedi and N. Afshordi, *J. Cosmol. Astropart. Phys.* **11**  
1048 (2019) 010.
- 1049 [69] J. Abedi and N. Afshordi, arXiv:2001.00821.
- 1050 [70] A. Testa and P. Pani, *Phys. Rev. D* **98**, 044018 (2018).
- 1051 [71] E. Berti, V. Cardoso, J. A. Gonzalez, U. Sperhake, M.  
1052 Hannam, S. Husa, and B. Bruegmann, *Phys. Rev. D* **76**,  
1053 064034 (2007).
- 1054 [72] V. Baibhav, E. Berti, V. Cardoso, and G. Khanna, *Phys.*  
1055 *Rev. D* **97**, 044048 (2018).
- 1056 [73] S. Bhagwat, M. Okounkova, S. W. Ballmer, D. A. Brown,  
1057 M. Giesler, M. A. Scheel, and S. A. Teukolsky, *Phys. Rev.*  
1058 *D* **97**, 104065 (2018).
- 1059 [74] A. Buonanno, G. B. Cook, and F. Pretorius, *Phys. Rev. D*  
1060 **75**, 124018 (2007).
- 1061 [75] A. Bohé *et al.*, *Phys. Rev. D* **95**, 044028 (2017).
- 1062 [76] A. Buonanno and T. Damour, *Phys. Rev. D* **59**, 084006  
1063 (1999).
- 1064 [77] A. Buonanno and T. Damour, *Phys. Rev. D* **62**, 064015  
1065 (2000).
- 1066 [78] R. Cotesta, A. Buonanno, A. Bohé, A. Taracchini, I.  
1067 Hinder, and S. Ossokine, *Phys. Rev. D* **98**, 084028 (2018).
- 1068 [79] E. Berti, V. Cardoso, and A. O. Starinets, *Classical*  
1069 *Quantum Gravity* **26**, 163001 (2009).
- 1070 [80] A. Taracchini *et al.*, *Phys. Rev. D* **89**, 061502 (2014).
- 1071 [81] F. Hofmann, E. Barausse, and L. Rezzolla, *Astrophys. J.*  
1072 *Lett.* **825**, L19 (2016).
- 1073 [82] N. Metropolis, A. W. Rosenbluth, M. N. Rosenbluth, A. H.  
1074 Teller, and E. Teller, *J. Chem. Phys.* **21**, 1087 (1953).
- 1075 [83] W. K. Hastings, *Biometrika* **57**, 97 (1970).
- 1076 [84] J. Skilling, *Bayesian Anal.* **1**, 833 (2006).
- 1077 [85] J. Veitch *et al.*, *Phys. Rev. D* **91**, 042003 (2015).
- 1078 [86] G. Ashton *et al.*, *Astrophys. J. Suppl.* **241**, 27 (2019).
- 1079 [87] R. J. E. Smith, G. Ashton, A. Vajpeyi, and C. Talbot, *Mon.*  
1080 *Not. R. Astron. Soc.* **498**, 4492 (2020).
- 1081 [11] [88] J. S. Speagle, *Mon. Not. R. Astron. Soc.* **493**, 3132  
1082 (2020).
- 1083 [89] B. P. Abbott *et al.* (KAGRA, LIGO Scientific, Virgo  
1084 Collaborations), *Living Rev. Relativity* **23**, 3 (2020).
- 1085 [90] D. H. Shoemaker, Technical Report No. LIGO-T1800044  
1086 (2010), <https://dcc.ligo.org/LIGO-T1800044/public>.
- 1087 [91] A. H. Mroue *et al.*, *Phys. Rev. Lett.* **111**, 241104 (2013).
- [92] H. Yang, K. Yagi, J. Blackman, L. Lehner, V. Paschalidis,  
F. Pretorius, and N. Yunes, *Phys. Rev. Lett.* **118**, 161101  
(2017).
- [93] A. Zimmerman, C.-J. Haster, and K. Chatzioannou, *Phys.*  
*Rev. D* **99**, 124044 (2019).
- [94] M. Isi, K. Chatzioannou, and W. M. Farr, *Phys. Rev. Lett.*  
**123**, 121101 (2019).
- [95] B. Carpenter, A. Gelman, M. D. Hoffman, D. Lee, B.  
Goodrich, M. Betancourt, M. Brubaker, J. Guo, P. Li, and  
A. Riddell, *J. Stat. Softw.* **76**, 1 (2017).
- [96] G. Carullo, arXiv:2102.05939 [Phys. Rev. D (to be  
published)].
- [97] K. Glampedakis and G. Pappas, *Phys. Rev. D* **97**, 041502  
(2018).
- [98] V. Cardoso and P. Pani, *Living Rev. Relativity* **22**, 4  
(2019).
- [99] E. Maggio, L. Buoninfante, A. Mazumdar, and P. Pani,  
*Phys. Rev. D* **102**, 064053 (2020).
- [100] V. Ferrari, M. Pauri, and F. Piazza, *Phys. Rev. D* **63**,  
064009 (2001).
- [101] C. Molina, P. Pani, V. Cardoso, and L. Gualtieri, *Phys. Rev.*  
*D* **81**, 124021 (2010).
- [102] P. Pani and V. Cardoso, *Phys. Rev. D* **79**, 084031 (2009).
- [103] J. L. Blázquez-Salcedo, C. F. B. Macedo, V. Cardoso, V.  
Ferrari, L. Gualtieri, F. S. Khoo, J. Kunz, and P. Pani, *Phys.*  
*Rev. D* **94**, 104024 (2016).
- [104] J. L. Blázquez-Salcedo, F. S. Khoo, and J. Kunz, *Phys.*  
*Rev. D* **96**, 064008 (2017).
- [105] R. Brito and C. Pacilio, *Phys. Rev. D* **98**, 104042 (2018).
- [106] G. Franciolini, L. Hui, R. Penco, L. Santoni, and E.  
Trincherini, *J. High Energy Phys.* **02** (2019) 127.
- [107] V. Cardoso, M. Kimura, A. Maselli, and L. Senatore, *Phys.*  
*Rev. Lett.* **121**, 251105 (2018).
- [108] O. J. Tattersall and P. G. Ferreira, *Phys. Rev. D* **97**, 104047  
(2018).
- [109] O. J. Tattersall, *Classical Quantum Gravity* **37**, 115007  
(2020).
- [110] J. L. Blázquez-Salcedo, S. Kahlen, and J. Kunz, *Eur. Phys.*  
*J. C* **79**, 1021 (2019).
- [111] H. O. Silva and K. Glampedakis, *Phys. Rev. D* **101**,  
044051 (2020).
- [112] K. Glampedakis and H. O. Silva, *Phys. Rev. D* **100**,  
044040 (2019).
- [113] J. L. Blázquez-Salcedo, C. A. R. Herdeiro, S. Kahlen, J.  
Kunz, A. M. Pombo, and E. Radu, *Eur. Phys. J. C* **81**, 155  
(2021).
- [114] J. L. Blázquez-Salcedo, D. D. Doneva, S. Kahlen, J. Kunz,  
P. Nedkova, and S. S. Yazadjiev, *Phys. Rev. D* **102**, 024086  
(2020).
- [115] P. A. Cano, K. Fransen, and T. Hertog, *Phys. Rev. D* **102**,  
044047 (2020).
- [116] P. K. Wagle, N. Yunes, and H. O. Silva, arXiv:103.09913.
- [117] L. Pierini and L. Gualtieri, arXiv:2103.09870 [Phys. Rev.  
D (to be published)].
- [118] K. Glampedakis, G. Pappas, H. O. Silva, and E. Berti,  
*Phys. Rev. D* **96**, 064054 (2017).
- [119] P. Jai-akson, A. Chatrabhuti, O. Evnin, and L. Lehner,  
*Phys. Rev. D* **96**, 044031 (2017).
- [120] P. Pani, E. Berti, and L. Gualtieri, *Phys. Rev. Lett.* **110**,  
241103 (2013).

- |      |   |      |
|------|---|------|
| 1148 | [121] P. Pani, E. Berti, and L. Gualtieri, <i>Phys. Rev. D</i> <b>88</b> , 064048 | 1168 |
| 1149 | (2013).   | 1169 |
| 1150 | [122] Z. Mark, H. Yang, A. Zimmerman, and Y. Chen, <i>Phys.</i>                   | 1170 |
| 1151 | <i>Rev. D</i> <b>91</b> , 044025 (2015).  | 1171 |
| 1152 | [123] O. J. C. Dias, M. Godazgar, and J. E. Santos, <i>Phys. Rev.</i>             | 1172 |
| 1153 | <i>Lett.</i> <b>114</b> , 151101 (2015).  | 1173 |
| 1154 | [124] M. Okounkova, L. C. Stein, M. A. Scheel, and S. A.                          | 1174 |
| 1155 | Teukolsky, <i>Phys. Rev. D</i> <b>100</b> , 104026 (2019).                        | 1175 |
| 1156 | [125] M. Okounkova, L. C. Stein, J. Moxon, M. A. Scheel, and                      | 1176 |
| 1157 | S. A. Teukolsky, <i>Phys. Rev. D</i> <b>101</b> , 104016 (2020).                  | 1177 |
| 1158 | [126] V. Cardoso, M. Kimura, A. Maselli, E. Berti, C. F. B.                       | 1178 |
| 1159 | Macedo, and R. McManus, <i>Phys. Rev. D</i> <b>99</b> , 104077 (2019).            | 1179 |
| 1160 | [127] R. McManus, E. Berti, C. F. B. Macedo, M. Kimura, A.                        | 1180 |
| 1161 | Maselli, and V. Cardoso, <i>Phys. Rev. D</i> <b>100</b> , 044061 (2019).          | 1181 |
| 1162 | [128] A. G. Suvorov and S. H. Völkel, <i>Phys. Rev. D</i> <b>103</b> , 044027     | 1182 |
| 1163 | (2021).   | 1183 |
| 1164 | [129] S. H. Völkel and E. Barausse, <i>Phys. Rev. D</i> <b>102</b> , 084025       | 1184 |
| 1165 | (2020).   | 1185 |
| 1166 | [130] S. H. Völkel, E. Barausse, N. Franchini, and A. E. Broderick,               | 1186 |
| 1167 | arXiv:2011.06812.   | 1187 |
|      | [131] D. Psaltis <i>et al.</i> (Event Horizon Telescope Collaboration),           | 1188 |
|      | <i>Phys. Rev. Lett.</i> <b>125</b> , 141104 (2020).                               |      |
|      | [132] H. Yang, <i>Phys. Rev. D</i> <b>103</b> , 084010 (2021).                    |      |
|      | [133] J. Healy, T. Bode, R. Haas, E. Pazos, P. Laguna, D.                         |      |
|      | Shoemaker, and N. Yunes, <i>Classical Quantum Gravity</i> <b>29</b> ,             |      |
|      | 232002 (2012).  |      |
|      | [134] E. Berti, V. Cardoso, L. Gualtieri, M. Horbatsch, and U.                    |      |
|      | Sperhake, <i>Phys. Rev. D</i> <b>87</b> , 124020 (2013).                          |      |
|      | [135] Z. Cao, P. Galaviz, and L.-F. Li, <i>Phys. Rev. D</i> <b>87</b> , 104029    |      |
|      | (2013).   |      |
|      | [136] M. Okounkova, L. C. Stein, M. A. Scheel, and D. A.                          |      |
|      | Hemberger, <i>Phys. Rev. D</i> <b>96</b> , 044020 (2017).                         |      |
|      | [137] E. W. Hirschmann, L. Lehner, S. L. Liebling, and C.                         |      |
|      | Palenzuela, <i>Phys. Rev. D</i> <b>97</b> , 064032 (2018).                        |      |
|      | [138] H. Witek, L. Gualtieri, P. Pani, and T. P. Sotiriou, <i>Phys.</i>           |      |
|      | <i>Rev. D</i> <b>99</b> , 064035 (2019).  |      |
|      | [139] M. Okounkova, <i>Phys. Rev. D</i> <b>102</b> , 084046 (2020).               |      |
|      | [140] W. E. East and J. L. Ripley, <i>Phys. Rev. D</i> <b>103</b> , 044040        |      |
|      | (2021).   |      |
|      | [141] S. Ossokine <i>et al.</i> , <i>Phys. Rev. D</i> <b>102</b> , 044055 (2020). |      |